ELSEVIER

Growth and magnetism of metallic thin films and multilayers by pulsed-laser deposition

J. Shen[a,*], Zheng Gai[b], J. Kirschner[c]

[a]*Condensed Matter Sciences Division, Oak Ridge National Laboratory, Oak Ridge, TN 37831-6057, USA*
[b]*Department of Physics & The State Key Laboratory for Mesoscopic Physics,
Peking University, Beijing 100871, PR China*
[c]*Max-Planck-Institut für Mikrostrukturphysik, Weinberg 2, 06120 Halle (Saale), Germany*

Abstract

Pulsed-laser deposition (PLD) is a powerful method to grow thin films and multilayers of complex materials such as transition metal oxides. In this case, the most cited advantage of PLD is the simplicity of preserving the stoichiometry of the target material. Recently, there are many reports showing that PLD can significantly improve the growth of even simple metallic thin films/multilayers. Here it is the ultrahigh instantaneous deposition rate and the high kinetic energy of PLD that play the most crucial roles. The improved growth, in particular for the first several monolayers, provides great opportunities to design artificial thin film structures that have promising physical properties.

Contents

* Corresponding author. Tel.: +1-865-2414828; fax: +1-865-5768135.
E-mail address: shenj@ornl.gov (J. Shen).

1. Introduction

Tailoring the properties of functional materials at atomic scale represents the ultimate goal in materials science research. The most desirable approach is to artificially fabricate structures with atomic precision, i.e. in layer-by-layer, row-by-row, or even atom-by-atom manner. For this purpose, in the past two decades, a great amount of effort has been devoted to improving growth techniques as well as growth simulations. The most noticeable reward came out of the research on two-dimensional magnetic ultrathin films and multilayers [1–3]. The ability to control thin film growth layer-by-layer has not only advanced our current understandings of two-dimensional physics, but also directly led to the observation of important and technologically relevant physical phenomena such as giant magnetoresistance (GMR) [4,5], tunneling magnetoresistance (TMR) [6,7], and ferromagnetism in dilute doped semiconductors [8–10]. GMR and TMR multilayers have already had a tremendous impact in magnetic data storage devices, and the magnetic semiconductors are defining a radically new avenue in spintronics [11–13].

Depending on the characteristics of materials and the cost concerns, several techniques have been employed for the growth of thin films and multilayers. These include thermal deposition (TD), sputter deposition (SD), chemical vapor deposition (CVD), and pulsed-laser deposition (PLD). Thermal deposition is the oldest and the most accessible technique to grow thin films. In its refined form, known as molecular beam epitaxy (MBE), thermal deposition is particularly useful for growing high-quality metallic and semiconductor films in a layer-by-layer manner. Typically MBE is conducted in an ultrahigh vacuum (UHV) environment, a necessary condition to keep the films free of contamination for basic science research. While MBE can also be used to grow multi-element thin films by

co-deposition from multiple sources, it is much less straightforward than the congruent transfer of multi-elemental materials by sputter deposition. The CVD method, which grows films on a substrate by decomposing a chosen precursor vapor, is preferred in industrial applications for its high and spatially homogeneous growth rates. CVD is also very useful to grow certain metastable thin films such as single crystal CrO_2 [14].

Compared to these growth methods, PLD has a unique capability to produce high-quality thin films of various kinds of materials (for a review, see [15]). The process of PLD involves focusing an intense laser pulse on the surface of a target, and removing target materials in the form of some volatile phases, e.g. a gas or a plasma. The distinct advantages of PLD include its simplicity of use, since the laser is totally decoupled from the growth chamber, and the ability to preserve the stoichiometry of compound materials under optimum conditions. The latter has made PLD the primary option for growing complex materials such as transition metal oxides, particularly after its first successful application in high-T_c superconductor thin films [16].

As for the growth of metallic thin films and multilayers, PLD has played a much smaller role so far. One may argue that this is partly due to its success in growing complex materials, and partly due to the maturity of other techniques such as MBE and sputter deposition in growing metallic systems. However, early experiments have shown that there are not any principle obstacles or challenges to grow metals with PLD [17,18]. More recent work has given strong evidence showing the superiority of PLD for layer-by-layer growth [19] as well as for growing high-quality thin films of refractory metals [20,21] and unstable alloys [22]. In particular, the successful application of PLD in magnetic ultrathin films and multilayers, which show clearly improved magnetic behavior as compared with similar MBE-grown structures [23], is making a compelling case that PLD should become a major force in the study of artificial metallic structures.

In this article, we review some recent developments in PLD growth of magnetic films and multilayers, which, in our opinion, represent the most significant impact of PLD in the fabrication of metallic systems. The readers are referred to previous review articles for some earlier work in this area [24,25]. Whenever possible, the growth and properties of PLD grown films are compared with those of MBE-grown films, since they both can be prepared in a UHV environment to greatly limit contamination effects. The paper is organized as follows: after some general discussions on fundamental issues related to PLD growth of metallic films in Section 2, we give extensive discussions on the ability of PLD to grow metastable structured magnetic thin films and alloys, as well as their corresponding magnetic properties in Section 3. The growth and magnetism of multilayers is described in Section 4, followed by some examples of the congruent deposition of multi-element thin films in Section 5. Section 6 is devoted to summarizing the most recent and promising applications of PLD in metallic systems. In the end (Section 7), we give conclusions and outlook.

2. Fundamental aspects of PLD growth of metals

2.1. General features of laser ablation of metals

In pulsed-laser deposition, also known as laser MBE when the growth is controlled and monitored in a layer-by-layer manner, an intense and short laser pulse strikes the target and ablates material from the target. Once the laser pulse is absorbed in the surface region of the target, the

electromagnetic energy is immediately converted into electronic excitations in the form of plasmons and unbound electrons. The excited electrons then transfer their energy to the lattice via electron–phonon (e–p) coupling within a few picoseconds. If the laser pulse duration is shorter than the e–p coupling, the conventional thermal deposition is significantly limited, other thermophysical effects start to play more important roles on the ablation threshold. Pronko et al. have shown that the interplay between the thermal gradient formed at vapor–surface interface and the one which extends into the bulk is a dominant factor in determining the ablation threshold [26]. Because femtosecond PLD is becoming increasingly attractive, we will give a more detailed discussion in Section 6.

In case τ is longer than the e–p coupling time, the e–p coupling leads to the material ablation that is exclusively via conventional heat deposition. For ceramic materials, the thermal diffusion length, given by $l = 2\sqrt{D\tau}$, where D is the thermal diffusion constant, is shorter than the optical absorption depth d. The bulk of the laser target will be heated down to the level of the optical absorption depth independent of pulse duration, making it possible to achieve significant material removal at lower laser fluence and with minimum ionization. The situation is reversed for metals, in which the optical absorption depth is smaller than the thermal diffusion length. The energy from the laser pulse will be first transferred into the absorption layer, and then thermally transported to the level of thermal diffusion length, which is proportional to $\sqrt{\tau}$.

For the most often used nanosecond (ns) pulsed-laser deposition by excimer lasers and Q-switched Nd-YAG lasers, the situation is complicated by ionization of the nascent erosion cloud before the laser pulse is over. With increasing laser fluence, the ablation process becomes more and more dominated by the laser-sustained plasma formation rather than by the simple surface heating. With sufficiently high laser fluence, the ps-scaled electron-lattice energy transfer allows significant surface vaporization after the first 100 ps of a nanosecond pulse. The vapor is subsequently ionized to form a plasma by the incoming photons during that pulse. The creation of the plasma then blocks the further energy transfer from the laser pulse to bulk materials underneath a certain depth, which equals the effective thermal diffusion length $l_{\mathrm{eff}} = 2\sqrt{D\tau_{\mathrm{eff}}}$, where τ_{eff} is the time needed to create an erosion plasma after the start of the laser pulse. This depth is typically several tens of nanometers for metals [27]. By absorbing the remainder of the laser pulse, the plasma is heated and accelerated, allowing the neutral atoms and ions to collide in the high-density region near the target (so-called Knudsen layer) and form a highly directional plasma expansion perpendicular to the surface. The plasma contains neutrals of a few eV in kinetic energies and ions that have kinetic energies up to a few hundred eV depending on the laser fluence. While the neutrals are slower than the ions, they both are considerably faster than the thermally evaporated atoms in traditional MBE growth ($\sim$0.1 eV). As will be addressed later, this difference in kinetic energy appears to be a major factor that gives rise to different growth in PLD and MBE.

For a given laser, in general, metals tend to require higher laser fluence for significant material removal than the ceramic materials. The actual ablation threshold, however, varies with types of metals depending on their cohesive energy and thermal conduction. The general trend is that the sp-bonded metals (Cd, Pb, etc.) have the lowest ablation threshold (a few 10 J/cm^2), the transition metals have an intermediate ablation threshold (1–2 J/cm^2), and the refractory metals (Mo, W, etc.) require the highest fluence for ablation ($\sim$10 J/cm^2). In general, setting the fluence at values slightly above the ablation threshold can significantly reduce the common problem of droplet formation in PLD, though the deposition rate is reduced as a trade-off.
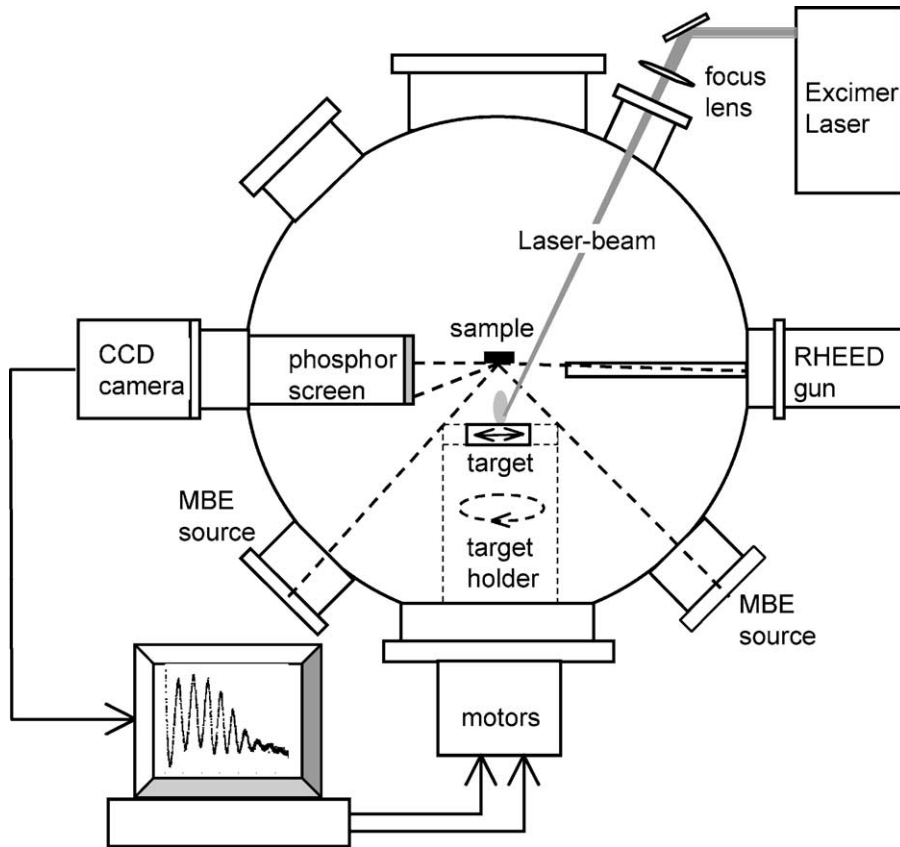
Fig. 1. Schematic drawing of a laser MBE setup. The RHEED system and a fully automated target carousel form the essential parts for the control of layer-by-layer growth of thin films and multilayers.

2.2. Growth of metallic thin films: PLD versus MBE

Traditionally, MBE has been a popular method for growing high-quality metallic thin films and multilayers. Because PLD can be applied to grow the same type of metallic films onto the same substrate at the same substrate temperature in the same ultrahigh vacuum environment as MBE does, it is of great interest to compare these two techniques in thin film growth. A typical UHV system equipped with facilities for both PLD and MBE growth is schematically shown in Fig. 1, which includes a reflection high-energy electron diffraction (RHEED) system that is used for monitoring the growth process in a "live" manner. After the growth, in most cases the samples are characterized in situ by various surface analytical tools including low energy electron diffraction (LEED), Auger electron spectroscopy (AES), scanning tunneling microscopy (STM), and magneto-optical Kerr effect (MOKE). It is also possible to study the structural and magnetic properties of the samples by ex situ methods after covering with a protecting layer, although great care has to be taken in understanding the influence of capping layers on magnetic properties.

The growth by PLD and MBE often yields drastically different morphology and structures of thin films. Here we present two examples in Figs. 2 and 3. Fig. 2 shows STM images (150 nm × 150 nm) of
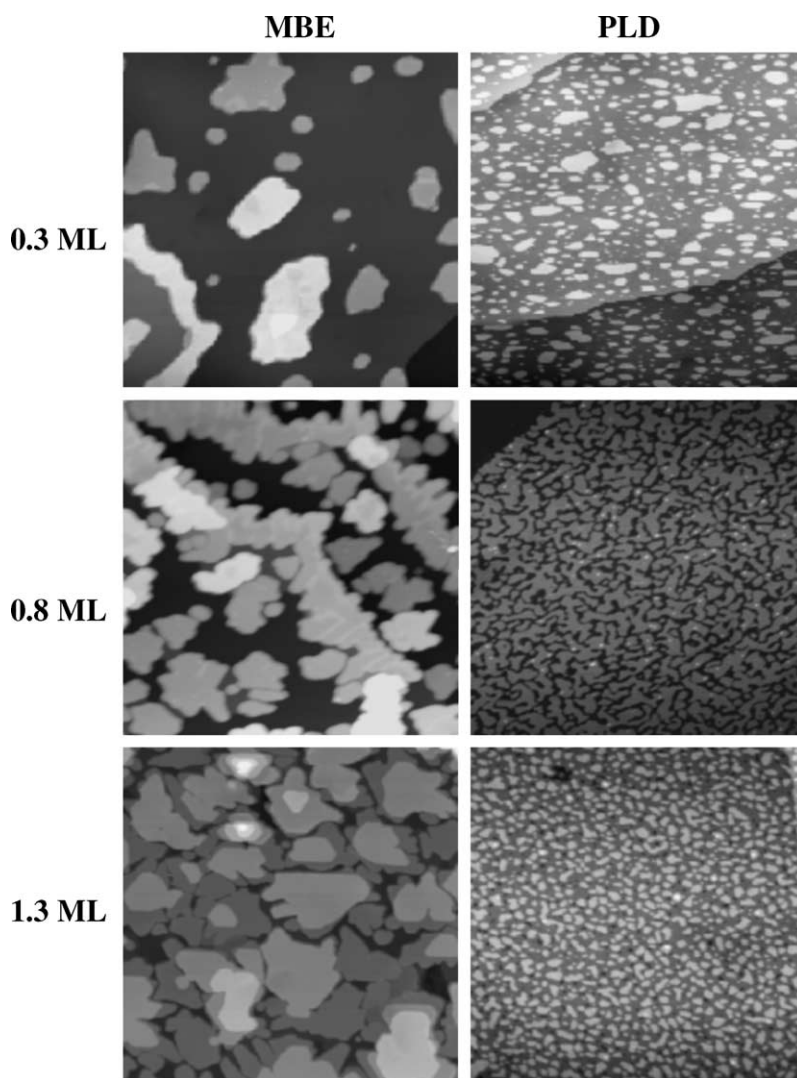
MBE **PLD**

Fig. 2.   STM images of in situ grown Co films on Cu(1 1 1) by MBE (left) and PLD (right) at various low thicknesses. The PLD films are much smoother than the MBE films as a result of a significantly improved two-dimensional growth.

low-thickness Co films grown by MBE (left) and PLD (right) on a single crystal Cu(1 1 1) surface. Note that both depositions were conducted in the same UHV system (5×10^{-11} mbar), at the same substrate temperature (230 K), with nearly the same average deposition rate ($\sim$0.2 ML/min). The MBE-grown Co films have the multilayer island morphology that leads to a significant roughness. In contrast, the PLD (KrF excimer, 248 nm, 5 Hz, 2 J/cm^2) films show almost ideal layer-by-layer morphology with high nucleation density. For example, at nominal thickness of 1.3 ML, the Cu(1 1 1) substrate is already completely wetted by the Co atoms. The STM images reveal no signs of dislocations or defects in the PLD films. There are also no observable droplets with a scanning electron microscope (SEM) because of the low fluence used in this study.
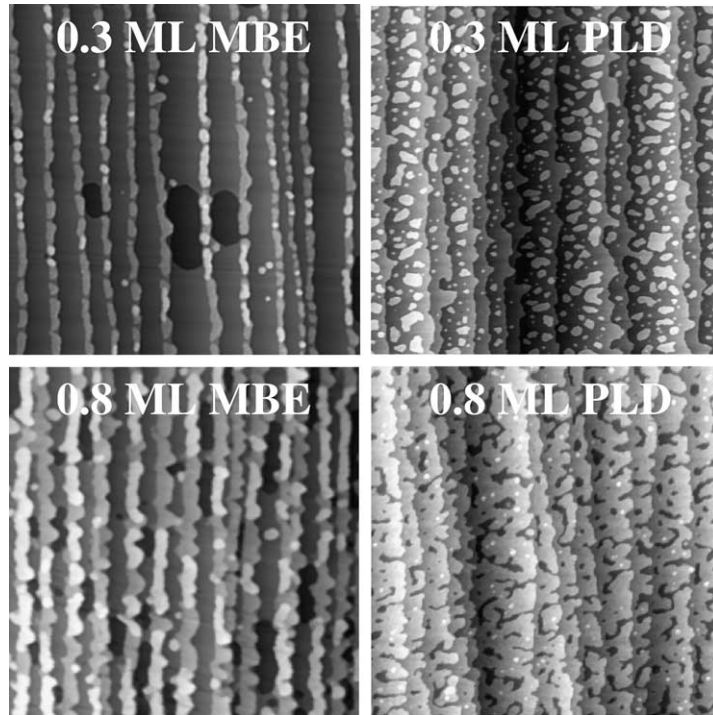
Fig. 3.   120 nm × 120 nm STM images of in situ grown Fe films on a vicinal Cu(1 1 1) substrate by MBE (left) and PLD (right). All Fe atoms are decorated along the step edges in the MBE films, while the PLD films are formed by two-dimensional islands on terraces of the substrate.

Fig. 3 shows STM images of Fe growth on a 1.2°-miscut Cu(1 1 1) substrate in the submonolayer regime by MBE and PLD. In the MBE growth, all Fe atoms have enough mobility to reach the step edges of Cu substrate and thus form parallel aligned stripes. The pulsed-laser-deposited Fe atoms all nucleate on the terraces of the Cu substrate, virtually ignoring the presence of the steps.

To understand why the two growth methods can have such different growth modes, it is worthwhile to analyze their characteristic features that are relevant to the growth. From a growth point of view, the two most important differences between PLD and MBE are:

(1) *Kinetic energy of deposits*: In PLD growth, it is known that the kinetic energy of ions can be as high as a few hundred eV at high fluence [28–31], though the neutral atoms are generally believed to have an order of magnitude smaller energy (a few eV). The ion energy can be limited below 100 eV if the laser fluence is chosen to be close to the ablation threshold. For example, at 1 J/cm^2, energies up to 100 eV have been measured for Fe [32]. At this fluence, a majority of the atoms and ions have kinetic energies of a few eV, and therefore defect formation, resputtering of atoms and mixing with the already deposited films is negligible. In contrast, by thermal evaporation the MBE generates neutral atoms with a kinetic energy of ∼0.1 eV per atom. In layer-by-layer PLD epitaxial growth, the high energy ions can be a concern due to the possible resputtering of the surface layers.

(2) *Instantaneous deposition rate*: Although PLD and MBE generally have similar average deposition rate, the pulsed nature of the PLD technique determines that there is a high instantaneous flux of atoms arriving on the substrate at each pulse. Even though the actual deposition time (∼μs) lasts longer than the pulse width (∼ns) for each laser pulse, the PLD still yields an instantaneous deposition rate of about 1000 ML/min or higher, which is several orders of magnitude higher than that of the MBE growth.

In the following, we shall see that these two differences in PLD and MBE can lead to drastically different growth modes for metallic thin films.

2.2.1. Nucleation

We start our discussion with the initial stages of growth, i.e. nucleation. Let us first consider the growth processes of PLD and MBE in a qualitative manner before we introduce more quantitative descriptions. The PLD growth can be simplified as a modulated flux that has a high rate (>1000 ML/min) during its very short "on" time (a few μs), followed by a much longer waiting time of ∼100 μs. The MBE growth, on the other hand, has a continuous flux with a rate ∼1 ML/min. Although the average deposition rate of PLD is about the same as that of MBE, during one laser shot the high evaporation rate of the laser and the small critical nucleus for metals on metals (two atoms mostly form a stable nucleus) lead to a high nucleation density. In the waiting period this scenario looks almost "frozen-in" until the next laser shot occurs. In reality, the nuclei are still mobile but at much lower speeds. Therefore some Ostwald ripening occurs, i.e. the agglomeration of small nuclei to larger islands, but the relatively high nucleation density persists. After the next laser pulse is triggered, the whole scene goes into motion again, with many "singles" diffusing around, but after a short time meeting 'slow' nucleation centers to reach the dock.

Now we consider the MBE growth at the same average deposition rate but with continuous flux. Because of the very low instantaneous deposition rate, on the time scale of 10 μs there are much less adatoms arriving at the sample surface as compared with the case of PLD. This means that the probability of forming critical nuclei on short distance is much reduced compared to PLD. In other words, each single Fe atom has time to wander a long path on the crystal before meeting a partner. This results in large distance between individual nucleation centers, i.e. in a low nucleation density.

On a more quantitative level, mean field nucleation theory [33,34] can be used to derive the stable island density n_x. Let us consider a simple case where 2D growth on a defect free surface, with dimers being stable and immobile (critical cluster size $i = 1$), without re-evaporation, and assuming isotropic diffusion characterized by its rate $D = D_0 \exp[E_d/k_B T]$, with E_d the diffusion barrier. For such a growth the density of monomers n_1 and of stable islands n_x ($x > 1$) can be obtained from the following two rate equations:

$$\frac{dn_1}{dt} = F - 2\sigma_1 D n_1^2 - \sigma_x D n_1 n_x - F(Ft - n_1) - F n_1 \tag{1}$$

$$\frac{dn_x}{dt} = \sigma_1 D n_1^2 + F n_1 \tag{2}$$

Eq. (1) states that the monomer density increases with flux F, but decreases with all incidents associated with diffusion and direct impinging. The density of stable islands, on the contrary, increases with dimer formation due to monomer diffusion or direct impinging. From Eqs. (1) and (2), one obtains the
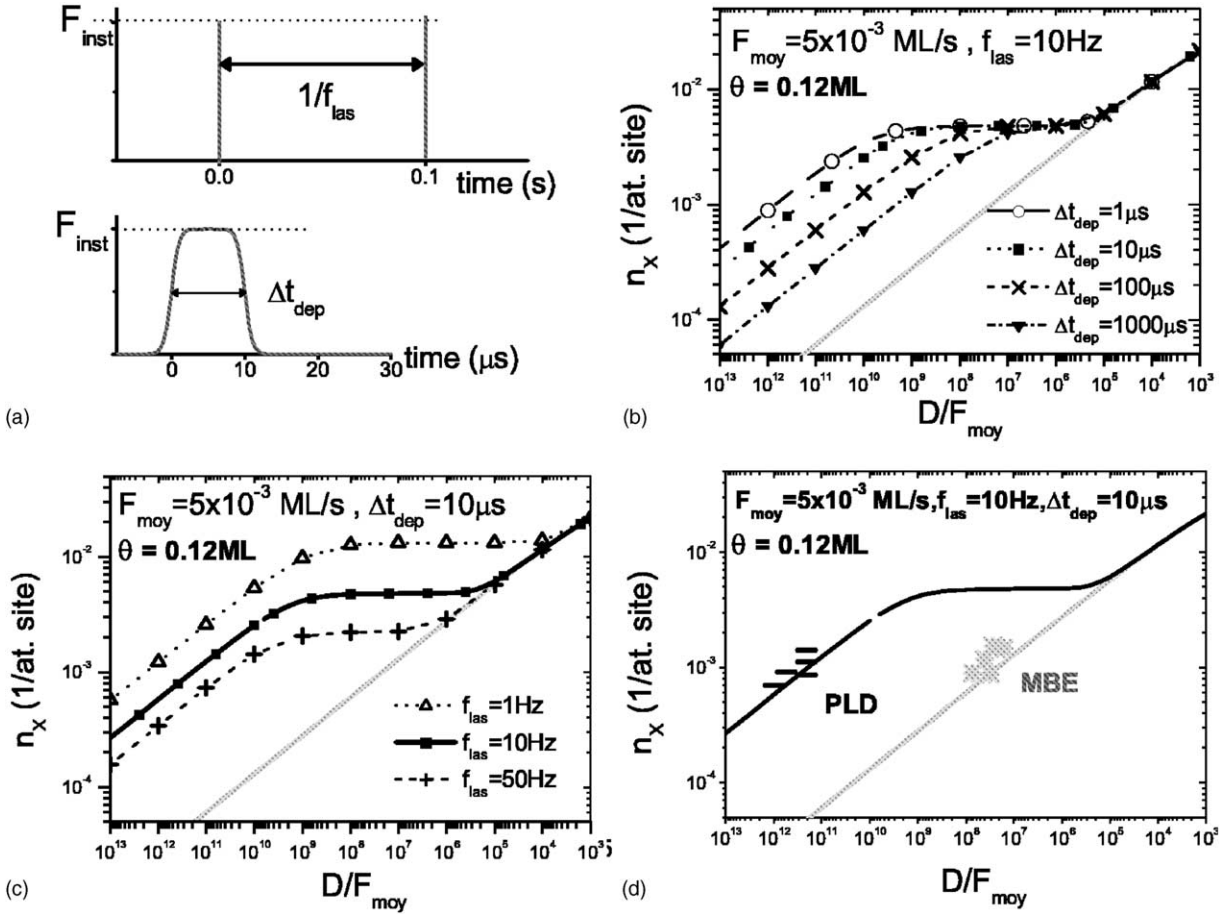
Fig. 4. (a) Time-dependence of deposition flux $F(t)$ used in the PLD deposition simulation; (b, c) island densities n_x calculated as a function of D/F for different deposition duration (Δt_{dep}) and laser pulse frequency (f_{las}); (d) comparison of the experimental PLD densities (black dashes) with the calculated n_x. The experimental MBE densities (gray stars) are put as a reference. Note for all the figures that the related calculation corresponding to MBE with the same flux F is also given by gray lines [35].

experimentally accountable island density

$$n_x = \eta(\Theta) \left(\frac{D_0}{F} \right)^{-\chi} \exp\left(-\frac{\chi E_d}{k_B T} \right) \tag{3}$$

where $\eta(\Theta) \cong \Theta^{1/3}$ is a coverage Θ dependent factor and χ is the scaling exponent that equals to 1/3. For PLD growth, the nucleation density depends also on the frequency and the pulse width in addition to the parameters in the above equations. The pulsed nature of PLD can be taken into account by solving the rate Eqs. (1) and (2) numerically. Recently Jubert et al. [35] have performed such calculations as shown in Fig. 4. Fig. 4(a) shows the time dependence of PLD flux used in simulation. Fig. 4(b) and (c) presents the calculated values of n_x (at $\Theta = 0.12$ ML and average deposition rate

$F_{moy} = 5 \times 10^{-3}$ ML/s) as a function of D/F for both PLD and MBE. The calculation clearly shows that n_x is strongly dependent on the deposition time per pulse (Fig. 4(b)) and PLD frequency (Fig. 4(c)). The calculations also indicate that for a given average deposition flux, n_x in PLD is larger than that in MBE, as far as the diffusion rate D is large enough to lead to a significant reduction of monomer density during period between two subsequent pulses. Only in cases when D/F is very low, i.e. the nucleation indistinguishably occurs during and between laser pulses, PLD and MBE have similar nucleation density. Fig. 4(d) gives the experimentally observed nucleation density as a function of D/F for both PLD and MBE-grown 0.12 ML Fe on Mo(1 1 0), which agree well with the calculated values from the mean field theory.

With the diffusion constant $D = 9 \times 10^7 \, s^{-1}$ for Co on Cu(1 1 1) [36], and the average deposition rate of 0.003 ML/s, the experiments in Fig. 2 were carried out at $D/F = 3 \times 10^{10}$. According to the simulated results in Fig. 4, under this condition PLD should produce at least an order of magnitude higher nucleation density than MBE. This is consistent with what has been observed in Fig. 2.

Comparative studies of the nucleation process of PLD and MBE have also been carried out extensively by computer simulations for cases that the pulse duration is either long [37,38], or short [39–41]. In a simplified model assuming zero pulse duration, infinitive D/F, and no step-edge diffusion barrier, Hinnemann et al. showed that PLD differs from MBE not only in the nucleation density, but also in the corresponding scaling behavior [39]. Fig. 5 shows their simulated results of nucleation density versus coverage at various pulse intensity in (a), and a snap shot of the island morphology in (b). For all coverages up to the maximum $\Theta = 1$ in the simulations, the nucleation density, $n(\Theta, I)$, is an increasing function of the pulse intensity I. The normalized nucleation density, $M(I, \Theta) = n(I, \Theta)/n(I, 1)$, was found to obey the scaling form

$$\ln M(I, \Theta) = \ln(I) g(z) \left(\frac{\ln(\Theta)}{\ln(I)} \right) \tag{4}$$

where the scaling function $g(z)$ is approximately a power law, $g(z) = Az^\beta$, with A being a constant and β ranging between 2.0 and 2.4 depending on the thickness. The logarithmic scaling function in Eq. (4) is distinctly different from the usual power law scaling function $f(x, y) = y^\alpha g(x/y^\beta)$, which holds in a limited coverage range for MBE growth [42,43]. This unusual scaling behavior for PLD, however, appears to be limited to the special case assumed in [39] ($D/F \rightarrow \infty$), since it was not observed in simulations of PLD with finite D/F values [40].

2.2.2. Layer-by-layer growth

The difference between PLD and MBE does not stop at the initial stages of growth. In fact, further increasing thickness can give rise to even more drastic contrast in their film morphology. As demonstrated in Fig. 6, for the same Co/Cu(1 1 1) system shown in Fig. 2, at higher thickness the MBE films feature mound-like islands that are tens of layers in height, while the PLD films still have a very good layer-by-layer morphology with at most three layers exposed for any given thickness below 6 ML. What happens to the films above 6 ML shall be discussed in Section 3.

To understand why PLD improves the growth in such a significant manner, it is useful to recall the two characteristic features of PLD, i.e. high kinetic energy and high instantaneous deposition rate. In the above we have already shown that high instantaneous deposition rate leads to high nucleation density. However, high nucleation density in PLD does not automatically lead to a better layer-by-layer growth, which relies on an efficient interlayer mass transport during the growth. This efficiency is
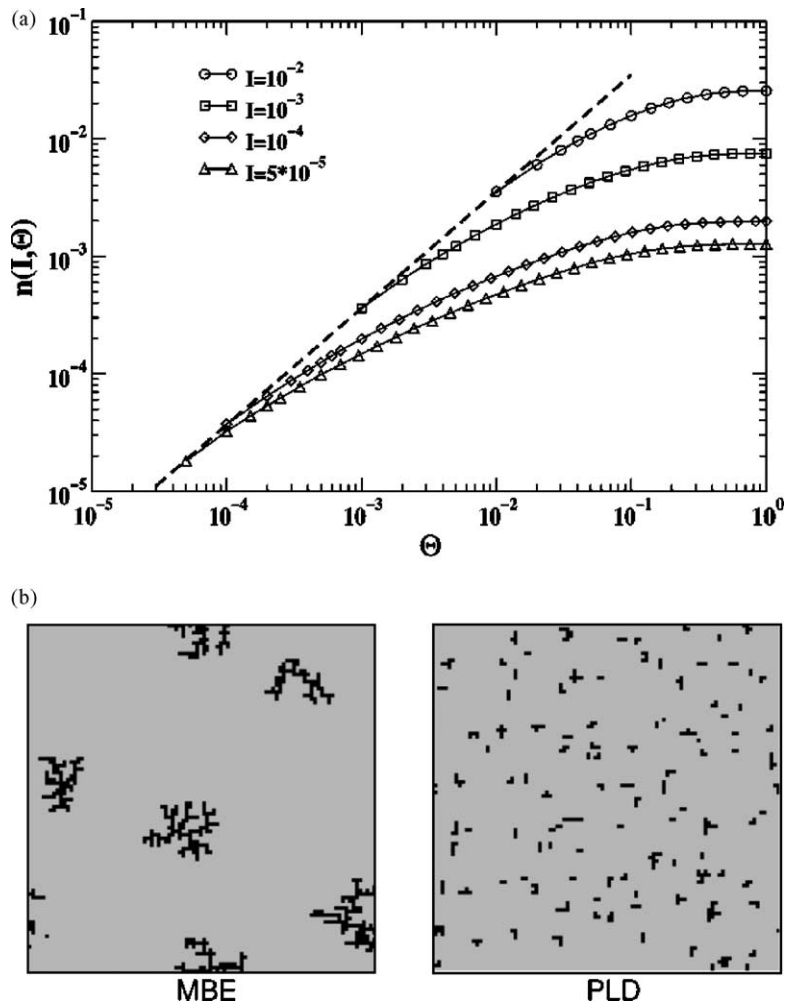
Fig. 5. (a) The nucleation density vs. time during the deposition of a monolayer. The dashed line has the slope 1. (b) Molecular beam epitaxy (left) compared to pulsed-laser deposition (right) for $D/F = 10^8$ and $I = 0.01$. The figure shows typical configurations after deposition of 0.05 monolayers (courtesy from D.E. Wolf).

determined by the probability as well as the number of attempts for an atom to hop from a higher to a lower level when encountering a step. In a given time, apparently the smaller the island is, the more attempts an atom on top will make to hop to a lower level. In the case of PLD, this trend however has to compete with the enhanced probability for nucleation events occurring on top of an island. In calculating the competition between these two factors, Hinnemann et al. [44] pointed out that PLD actually would lead to a rougher surface than MBE does if $D/F \rightarrow \infty$. Even at finite D/F, this trend only reverses when an unrealistically large step-edge barrier (Ehrlich–Schwoebel barrier) is assumed. Therefore, the experimentally observed layer-by-layer growth in PLD of Co/Cu(1 1 1) (Fig. 6) and some other systems [45] may not be a direct consequence of the high nucleation density, although it has been argued that the smaller islands in PLD films would make it easier to smooth the films by post-growth thermal annealing [46].
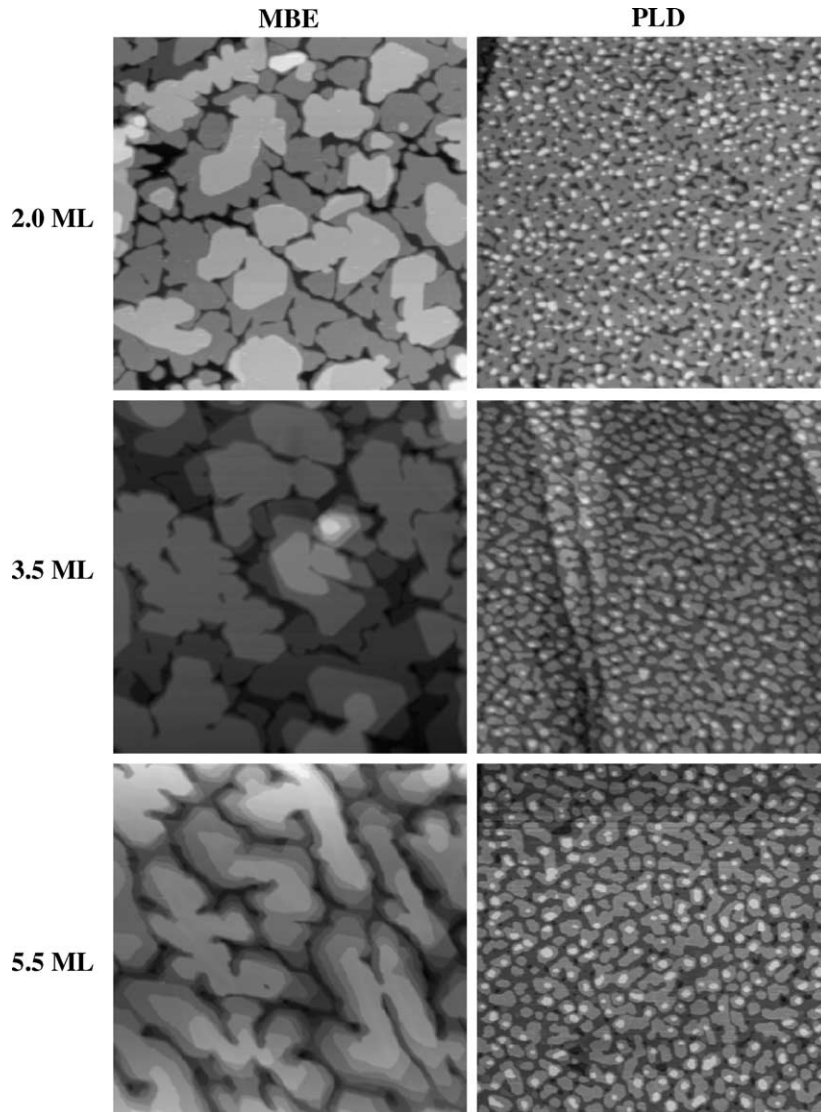
MBE	PLD

Fig. 6. STM images of in situ grown Co films on Cu(1 1 1) by MBE (left) and PLD (right) at higher thicknesses than those shown in Fig. 2. The PLD films preserve the morphology of layer-by-layer growth, while the MBE films feature multilayer-high islands.

The improved layer-by-layer growth in PLD can be, to some extent, benefited from the presence of a large number of small islands, which may enhance the hopping probability for an atom on top. This hopping probability is described by the Arrhenius expression

$$p = \left(\frac{v_s}{v_t\, e^{-\Delta E_s/kT}} \right) \tag{5}$$

where v_s is the prefactor at the step edge, v_t the prefactor on the terrace, and ΔE_s the step-edge barrier. Although calculation has shown that ΔE_s has a tendency to increase with increasing island size, it hardly varies when the island size becomes four atoms wide or larger [47]. Therefore, for any two-dimensional growth, the effect of island size on step-edge barrier should be diminished when coverage is above 0.5 ML, at which the coalescence of the islands becomes dominant. The fact that the PLD film (in Fig. 2) has nearly no second layer nuclei even at 0.8 ML indicates that the layer-by-layer growth does not only originate from the (small) island size induced reduction of the step-edge barrier.

This leads to the other important feature of PLD growth, i.e. the relatively high kinetic energy of depositing species. As mentioned, for the laser fluence set at slightly above the ablation threshold, PLD growth involves a combination of neutrals and ions with kinetic energies of a few eV and a few tens eV, respectively. These energies can influence the growth by enhancing the transient mobility of adatoms, or introducing some local defects. The transient mobility comes from the local surface lattice heating due to the combined contributions of latent heat of condensation and kinetic energy dissipation. For MBE growth, the kinetic energy dissipation is negligible, while for PLD growth these two contributions are very comparable. The increased local surface heating, even though it is highly localized both temporally ($\sim$ps) and spatially (one or two atomic lattices) [48], may nevertheless be sufficient to enhance the probability for an adatom to make a jump to another lattice site, which is beneficial for layer-by-layer growth. Molecular dynamic simulations of homoepitaxial growth of Ag/Ag(1 1 1) [49] and Cu/Cu(1 0 0) [50] indicated that increasing the atom energy from 0.1 to 10 eV changed the growth mode from three-dimensional to layer-by-layer. The primary mechanism for the improved layer-by-layer growth was attributed to the displacement of atoms from unstable positions to stable positions by the immediate ballistic impact of high-energy incidents. Another molecular dynamic simulation on heteroepitaxial system of Co/Cu(1 0 0) showed that incoming atoms with kinetic energy over 3 eV enhance the exchange diffusion and lead to improved layer-by-layer growth [51].

Another role of the high kinetic energy of the incident atoms is to create local defects. The effect of local defects is mostly increasing nucleation density. When other growth conditions remain unchanged, enhanced nucleation allows more attempts for adatoms to descend to the lower level, which should assist two-dimensional growth in a similar manner to that of an ion sputtering assisted growth [52,53]. However, this effect may only become noticeable when the portion of the ions is significant, since the high instantaneous rate would lead to a high nucleation density anyway.

3. PLD growth of metastable structured films

The high instantaneous rate, and the high quenching rate in PLD means that the growth proceeds in conditions very far from equilibrium. Under optimum conditions, it is possible to grow thin films with highly metastable structures that are hard to stabilize by other deposition techniques. A good example can be found in the growth of polycrystalline Ag_xNi_{1-x} solid solutions by PLD [54]. In spite of the disagreement on the maximum concentration of Ag in the solid solution [55,56], Ag_xNi_{1-x} could only be obtained in amorphous phase at best by any other techniques due to its unusually strong tendency towards demixing [57]. The ability to stabilize otherwise unstable structures is probably the biggest advantage of using PLD to grow metallic systems. In this section, we introduce several detailed examples to show the PLD growth of layered metastable structures for both single element and binary alloys, and their corresponding magnetic properties as well.

3.1. Growth and magnetism of fcc γ-Fe

One of the most famous metastable phase is fcc γ-Fe. In the past, the γ-Fe phase has attracted great attention both because of its lattice constant-dependent rich magnetic phases [58–60], and because of its intimate tie to the steel formation process. While γ-Fe does not exist at temperatures below 914 °C in natural bulk form, it can be stabilized at room temperature either by quenching γ-Fe precipitates in a Cu matrix [61], or by epitaxial growth on a fcc substrate such as Cu [62]. Due to the high metastability, in clean UHV environment the growth of fcc Fe films on Cu lasts not more than 10 ML before a fcc → bcc phase transformation occurs [2]. This fcc → bcc transformation can be significantly delayed when using a small amount of carbon + oxygen to assist the growth [63]. Recently, it has been shown that Fe_xMn_{1-x} buffer layers can be used to stabilize the fcc Fe phase up to a higher critical thickness [64].

So far most of the work on fcc Fe films has been carried out using MBE growth. A feature of this growth is the early formation of bcc-like stripes and needles. These bcc-like structures appear to strongly affect the magnetic properties of Fe films on both Cu(1 0 0) and Cu(1 1 1) substrates. The PLD Fe/Cu films, however, appear to have a much more fcc-like structure at low thicknesses.

3.1.1. Fe on Cu(1 0 0)

In magnetic ultrathin film systems, Fe/Cu(1 0 0) is by far the most investigated, and, accordingly, most disputed system in terms of almost every aspect of its structural and magnetic properties. After nearly a full decade of research by numerous groups, just when people start to believe that a clear picture of the correlation between structure and magnetism has emerged, new reports on both structure and magnetism indicate the situation is quite otherwise. Below, we first briefly review the up-to-date development on the investigation of the structural and magnetic properties of the MBE-grown Fe/Cu(1 0 0) films, and then make direct comparison between PLD and MBE films.

After Thomassen et al. [65] and Li et al. [66], the room temperature grown Fe/Cu(1 0 0) films by MBE are usually divided into three regions based on their magnetic behavior. Fig. 7 shows the magnetic phase diagram determined by magneto-optical Kerr effect (MOKE) measurements. In region I (0–4 ML), the films are considered as uniformly magnetized with high magnetic moment of $2.5\mu_B$ [67,68], and the easy magnetization axis is perpendicular to the film plane. In region II (5–10 ML), the films are only ferromagnetic in the surface layers, while the layers underneath are in some kind of antiferromagnetic spin structure [66,69]. In region III (>10 ML), the films become again uniformly magnetized with an easy magnetization axis lying in the film plane.

The structural origin of such complex magnetic behavior has also been investigated extensively. The high-spin phase in region I was initially believed to be associated with a tetragonal distortion of the fcc phase (fct) that effectively expands the atomic volume [70]. Low energy electron diffraction reveals "(1 × 4)"- and "(1 × 5)"-like patterns that were attributed to atomic buckling both in the plane and along the surface normal. Recently an STM work gave strong hints that the films in region I have mixed phases of bcc and fcc structures [71], and the observed LEED superstructure spots are trademarks of the strained bcc-like phase. It is suggested that the bcc part of the films is the real contributor to the high-spin phase. In region II, all but the top layers become pseudormophic or fcc-like, which is known to have an antiferromagnetic ground state in bulk. The top layers remain ferromagnetic due to the tetragonal distortion. The magnetic properties of films in region III correspond to those of transformed bcc Fe films.
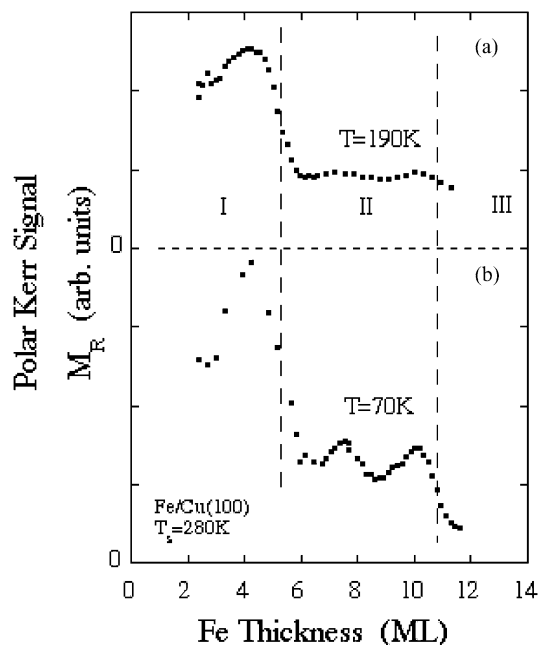
Fig. 7. Remanent magnetization (M_R) from polar MOKE vs. thickness across an Fe wedge grown at substrate temperature of 280 K and measured at 190 K (a) and 70 K (b). Regions I and III correspond to ferromagnetic phases, while region II has a live surface ferromagnetic layer. The M_R oscillations are attributed to the antiferromagnetic Fe layers underneath (courtesy from D. Li).

The PLD grown Fe/Cu(1 0 0) films display different morphology and structure. Fig. 8 shows the PLD film morphology of initial stages of growth recorded by STM. Near ideal two-dimensional growth is established in the submonolayer regime, where practically no second layer nuclei are visible. This is in stark contrast to the morphology of MBE Fe/Cu(1 0 0) films. For comparison, an STM image of a 0.7 ML MBE-grown film is included as an inset in Fig. 8(c) (0.7 ML PLD film). Apparently, the MBE film has significantly more second layer nuclei (bright spots) and thus a much less ideal two-dimensional growth mode than that of PLD. This is consistent with what we have discussed in Section 2 on the differences between these two growth techniques.

The layer-by-layer growth of the PLD films proceeds with increasing thickness up to 10 ML, above which the films transform into bcc structures and become very rough [72,73]. While the MBE and the PLD films transform into bulk-like bcc structures at similar thickness of 10 ML, it remains a matter of dispute whether the strained bcc-like structures exist in the PLD films at the early stages of growth. According to our own LEED study [72,73], as shown in Fig. 9, the (5×1) superstructure spots, which are the trademarks of the strained bcc-like structures in MBE films according to [71], are missing in the LEED patterns recorded from PLD films below 4 ML thickness. The 3 ML PLD film has similar (1×1) LEED pattern and $(0, 0)$ spot *I/V* curve to those of the clean Cu(1 0 0) substrate. In contrast, the MBE film prepared in the same UHV system clearly displays a (1×4)-like pattern. A later LEED investigation [74], however, showed that the (5×1) superstructure spots are visible in the LEED patterns. Although the real structures need to be further investigated, it is safe to claim that the (1×1) LEED patterns that we observed (in Fig. 9) were not from surface contamination due to carbon or
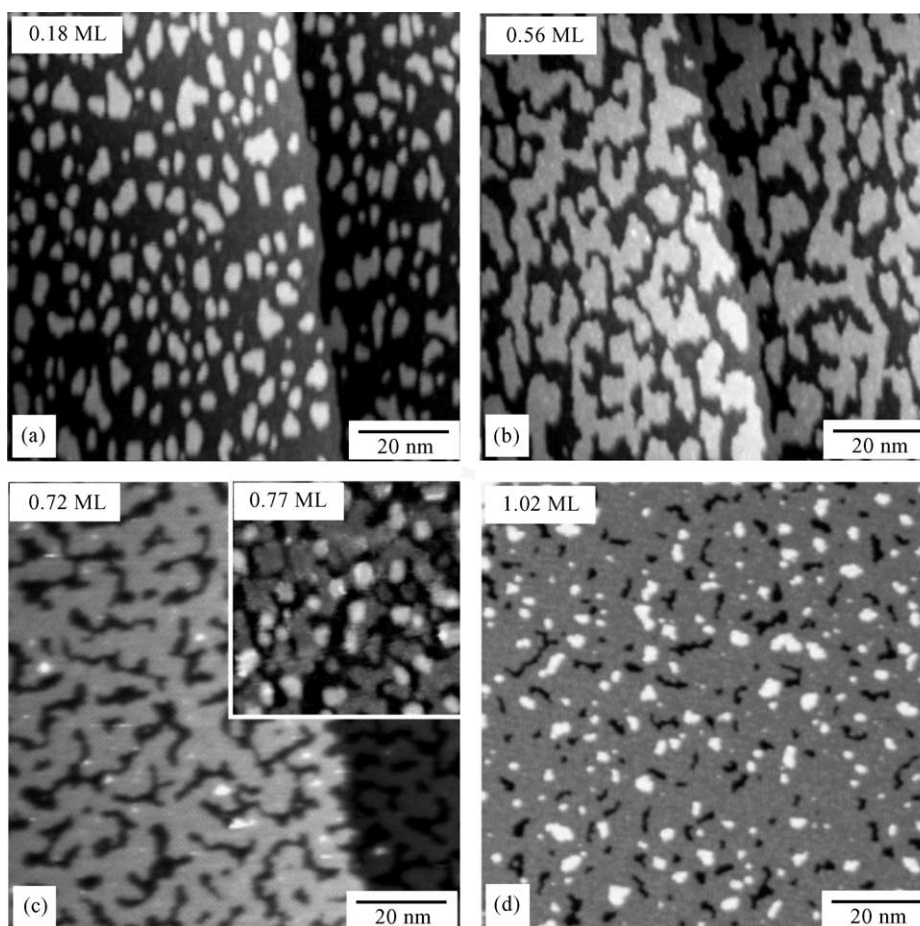
Fig. 8.   (a) and (b) STM images of the initial stages of growth of Fe/Cu(1 0 0) by pulsed-laser deposition, clearly demonstrating layer-by-layer growth from the initial stages. There are less than 5% of both the substrate surface and second ML, visible in nominally 1 ML-thick pulsed-laser-deposited Fe/Cu(1 0 0). The inset in (c) shows part of a STM image of thermally deposited Fe/Cu(1 0 0) of a similar coverage than (d) on the same lateral scale, clearly displaying the poor growth in thermal deposition indicated by the significant coverage already present in the second ML at this thickness.

oxygen, since these elements would introduce a c(2×2) reconstruction on the surface [75]. Other than some unknown issues related to growth conditions, it is possible that the superstructures in the PLD films are highly metastable and the films soon recover the more stable (1×1) structure after a short time at room temperature.

The magnetic properties of the PLD Fe/Cu(1 0 0) films are also very complicated as featured by multiple phase transitions. Fig. 10 shows the magnetic phase diagram determined by in situ MOKE from the PLD Fe films. Depending on the magnetic anisotropy, we may divide the growth of the films into five stages. In stage I (0–2 ML), the films have a perpendicular easy magnetization axis. A spin reorientation occurs at about 2 ML leading to an in-plane magnetization for films in stage II (2–5 ML). Between 5 and 7 ML (stage III), the films undergo a reversed spin reorientation from in-plane to perpendicular. In this thickness regime the films have both perpendicular and in-plane
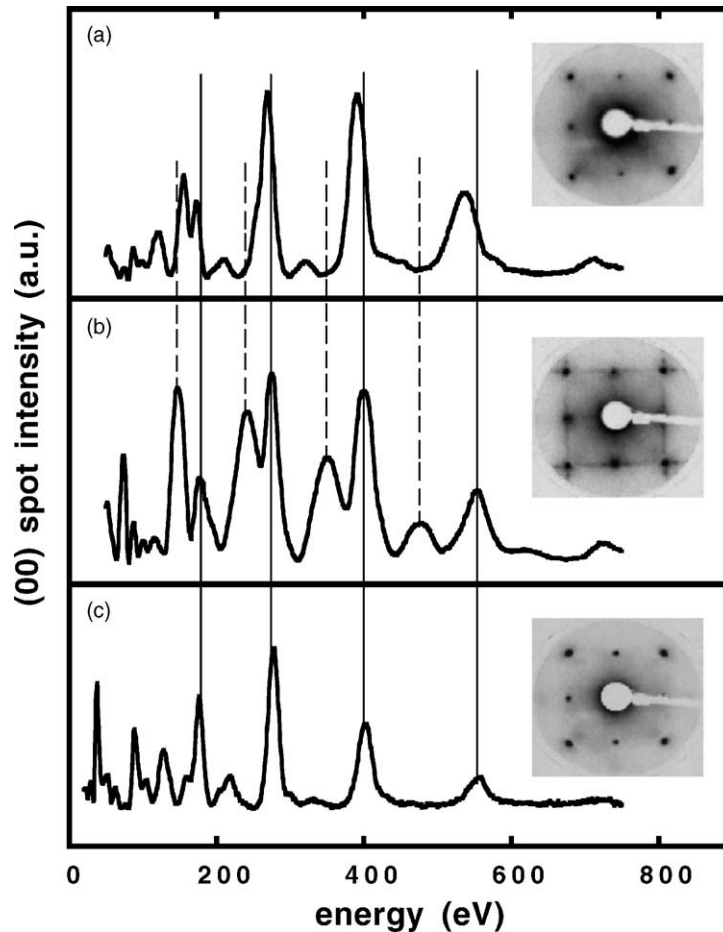
Fig. 9. Low-energy electron diffraction data from two 3 ML-thick Fe films on Cu(1 0 0), prepared by pulsed-laser deposition (a) and thermal deposition (b). The LEED data of clean Cu(1 0 0) substrate is shown as a reference in (c). Insets are the LEED patterns taken at 105 eV. The curves give the intensity of the specular beam as a function of the energy at near-normal incidence. Both fct (dashed lines) and fcc (solid lines) families of peaks are visible in the thermal deposition film, while in the pulsed-laser deposition film only fcc peaks are present. The LEED pattern of the pulsed-laser deposition film is (1×1) in similar to that of Cu(1 0 0) substrate, whereas the thermal deposition film has a (5×1) superstructure.

magnetization components. The films then become fully perpendicularly magnetized in stage IV (7–10 ML). Above 10 ML (stage V), the films are again in-plane magnetized corresponding to the formation of bcc structure. The characteristic magnetic hysteresis loops recorded from each stage are shown in Fig. 11.

Along with these complex spin reorientations, the characteristic "uniform to non-uniform" spin phase transition for the MBE films is also present in the PLD films, except with a clearly different spin structure in the transformed phase. As shown in Fig. 10, the saturation Kerr intensity increases linearly with thickness below 4 ML, indicating that the films are uniformly magnetized. Since the Kerr intensity of the PLD films is very comparable to that of the MBE films in the same thickness regime [72], the
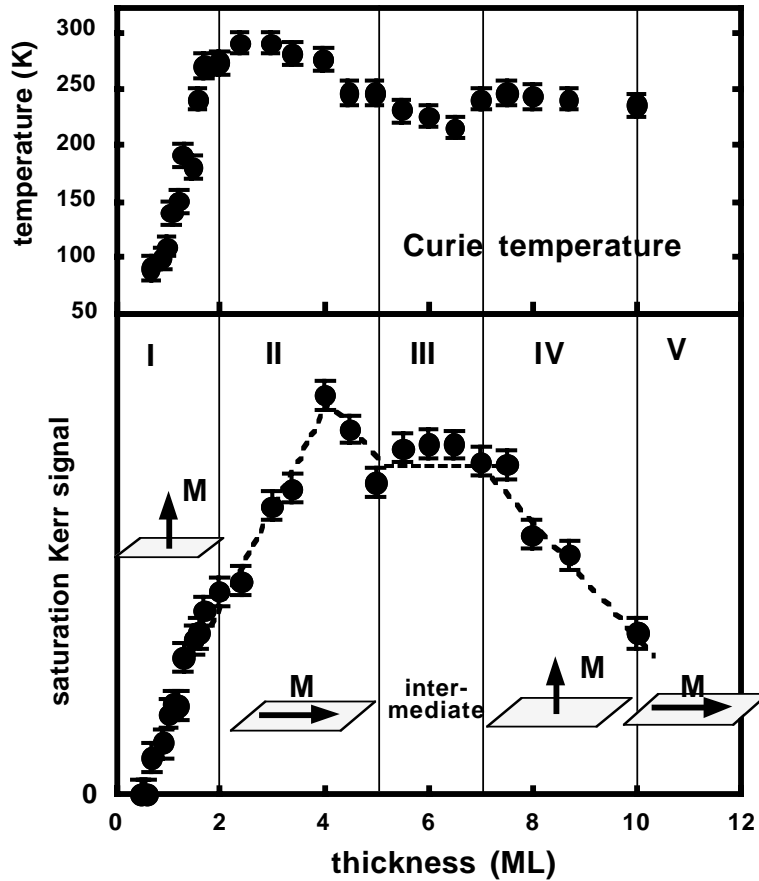
Fig. 10. Plots of Curie temperature (upper panel) and saturation magnetization (lower panel) vs. thickness of the pulsed-laser-deposited Fe/Cu(1 0 0) films. Depending on the magnetic anisotropy, five regions can be distinguished with the corresponding easy magnetization axis schematically shown in the figure. From 0 to 4 ML, the films are uniformly magnetized. Between 4 and 10 ML, the films have multiple magnetic phases coexisting. Above 10 ML, the films become ferromagnetic again due to the fcc → bcc transition.

PLD films should also be in a high-spin phase. Above 4 ML, the Kerr intensity drops almost monotonically except a small plateau region between 5 and 7 ML. This behavior is different from that of the MBE Fe/Cu(1 0 0) films (see Fig. 7), of which the Kerr intensity stays around a constant value due to the ferromagnetic live layers in the surface region only. Therefore, one may conclude that while the PLD films are also in a non-uniform spin phase above 4 ML, the spin structures of the PLD films are not the same as those of the MBE films. It is not possible to determine the actual spin structures of the PLD films (>4 ML) based on the MOKE measurements given the on-going multiple magnetic and structural phase transitions in this thickness regime. Since there is a high degree of possibility that magnetic inhomogeneties exist in the lateral direction, magnetic probes with high spatial resolution, such as scanning electron microscope with spin polarization analysis (SEMPA) and spin polarized low energy electron microscope (SPLEEM), can be very useful to obtain in-depth information of the magnetic phases in the PLD films.
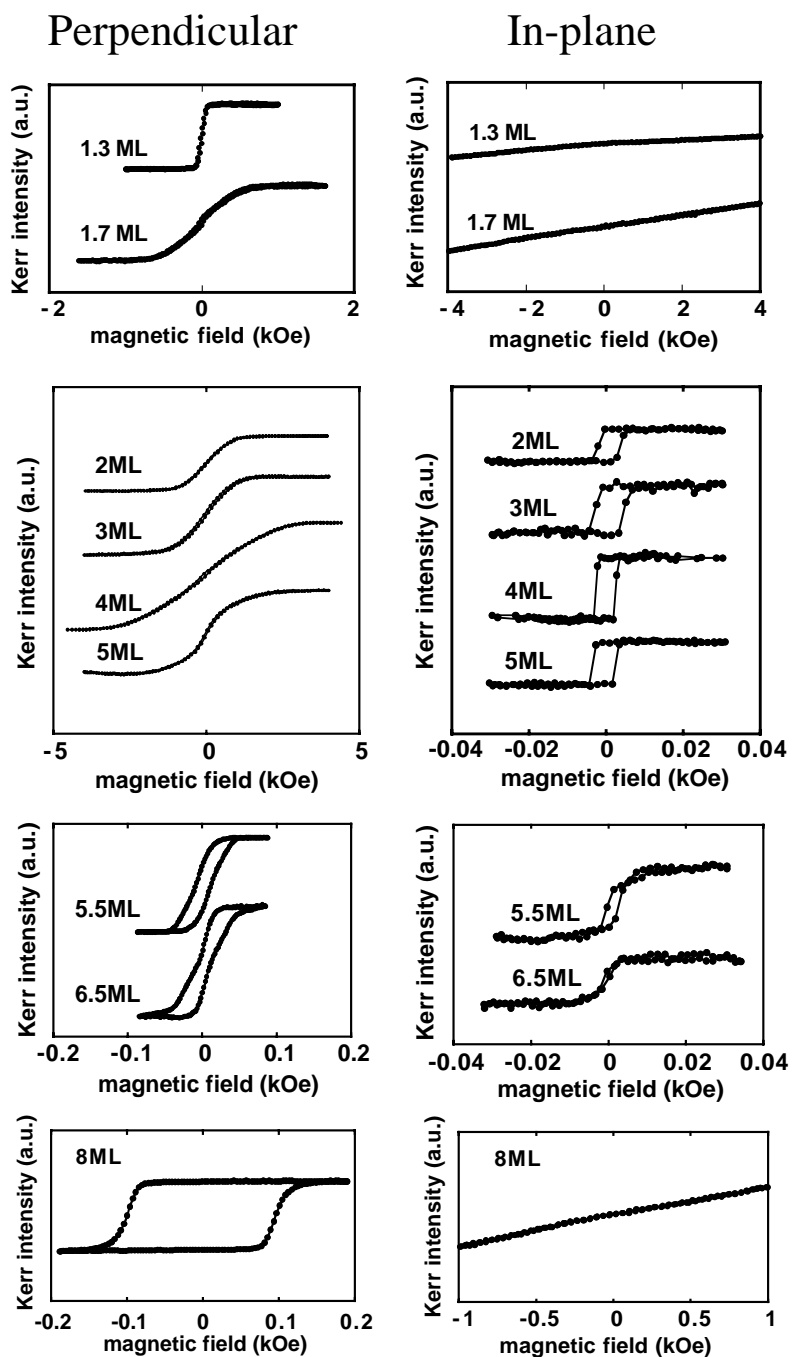
Fig. 11. Perpendicular (left) and in-plane (right) magneto-optical Kerr effect hysteresis loops of pulsed-laser-deposited Fe/Cu(1 0 0) films at various thicknesses. With increasing thickness, the easy magnetization axis changes from perpendicular (<2 ML), to in-plane (2–5 ML), and canted (5–7 ML) back to perpendicular (7–10 ML). Note that the scales of magnetic field are different and the units of Kerr intensities are different for polar and in-plane magnetization.
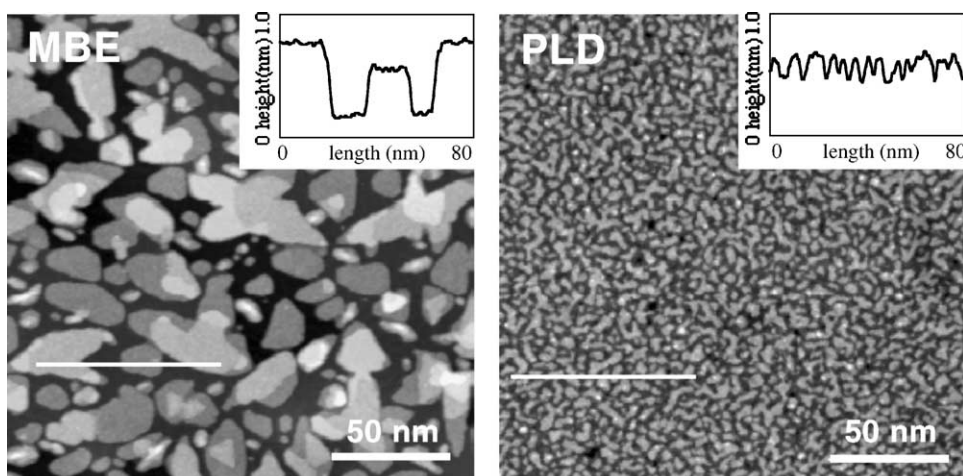
Fig. 12. STM topography images of 1.6 ML Fe/Cu(1 1 1) films prepared by MBE (left) and pulsed-laser deposition (right). The thermally deposited films grow in a multilayer mode that features both bilayer and trilayer islands, as indicated by the inset line profile picture. The pulsed-laser-deposited film shows a typical morphology of good layer-by-layer growth.

3.1.2. Fe on Cu(1 1 1)

In general, layer-by-layer growth on a fcc(1 1 1) substrate is rather difficult due to the potential formation of fcc/hcp stacking faults or fcc twin boundaries in addition to the usual step-edge barrier. These structural defects are caused by the mismatching lattice between islands that are nucleated at the two different sites, often referred to as A and B sites [76]. Here we show that the fcc/hcp stacking faults can be effectively removed when using PLD to grow the Fe films on Cu(1 1 1) substrate. Consequently, a good layer-by-layer growth prevails.

Fig. 12 shows STM images of 1.6 ML Fe/Cu(1 1 1) films grown by MBE and PLD at 220 K. At 1.6 ML, the MBE film still has a large fraction of surface area exposed to the substrate level, and the Fe islands, correspondingly, are typically three to four layers high as indicated by the marked line profile. In contrast, the PLD film has fully wetted the substrate with only two layers exposed (first and second), a clear indication of an ideal two-dimensional growth. Increasing thickness results in even larger discrepancy in film morphology, as the PLD films proceed in a layer-by-layer mode and the MBE films become increasingly rough. Side-by-side comparison of the morphology between PLD and MBE Fe/Cu(1 1 1) films at 3.5 and 5.5 ML is shown in Fig. 13.

Other than the mound-like islands, a noticeable feature in the MBE films is the continuous evolution of some ridge-like structures. These $\langle 1\,1\,0 \rangle$-oriented ridge-like features, after an analysis of the combined data from STM and LEED, were identified as the morphological appearance of bcc(1 1 0) structures with Kurdyumov–Sachs orientations [77]. In fact such ridge-like features are already visible in the 1.6 ML MBE film, as shown in Fig. 12. We have not observed similar bcc ridges in the PLD films below 6 ML thickness. Above this thickness, some bcc "needles" start to appear, and become dominant above 10 ML [78].

The most direct evidence indicating that the PLD films have more stable fcc phase than the MBE films is given by quantitative LEED analysis. The calculated average interlayer distance versus thickness for both types of films is shown in Fig. 14. The shaded area represents the thickness regime of
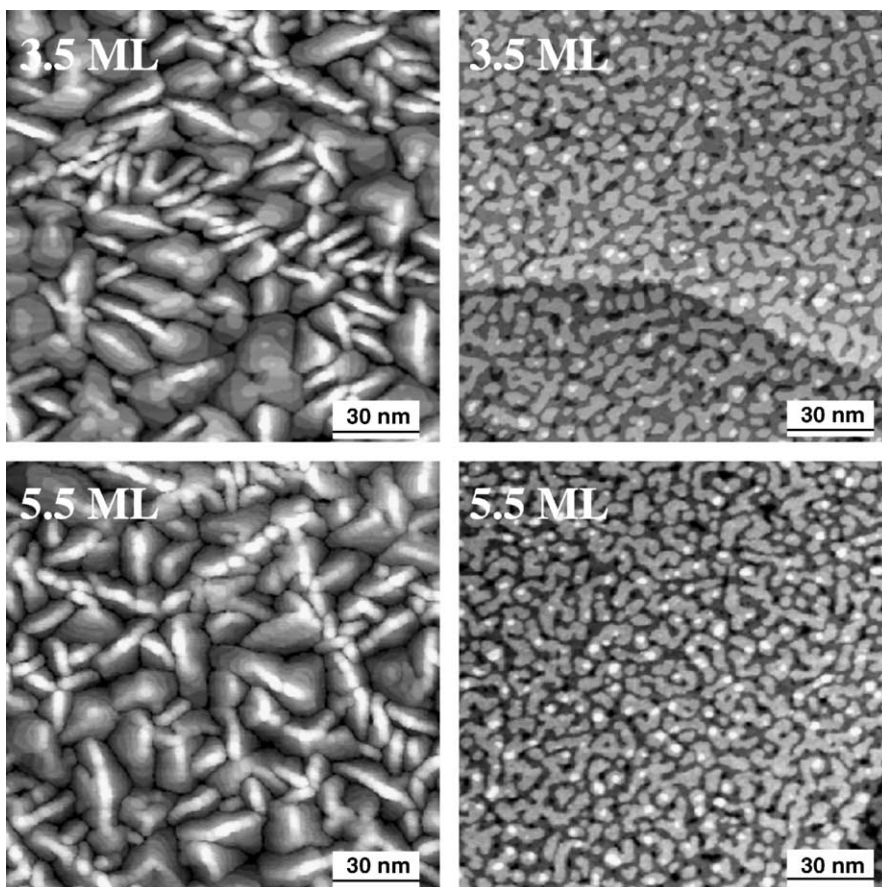
Fig. 13. STM topography images of Fe/Cu(1 1 1) films prepared by MBE (left column) and pulsed-laser deposition (right column). Above 3 ML, the morphology of the MBE films is dominated by ridge-like bcc structures. The pulsed-laser-deposited films show typical morphology of a good layer-by-layer growth without the appearance of the bcc structures.

bcc(1 1 0) structure, which has a smaller interlayer distance than that of the fcc(1 1 1) Fe structure. The LEED patterns for the fcc and bcc Fe films are included as insets in the corresponding places. Consistent with the STM observations, the LEED data show that the PLD films do not have the presence of the bcc structures below 6 ML. The thickness for the fcc → bcc transition is reduced to 3 ML for the MBE-grown films, with a high degree of morphological imperfections.

The morphological and structural differences between the PLD and the MBE films have significant consequences on their magnetic properties. The easy magnetization axis is perpendicular to the film plane for both types of films at low thickness, and reorients to the in-plane direction at about 2 and 3 ML for the PLD and the MBE films, respectively. The spin reorientation of the MBE films is associated with the fcc → bcc structural phase transition, similar to what has been observed in the Fe/Cu(1 0 0) films. The spin reorientation of the PLD films, however, has nothing to do with any structural transitions since the films remain fcc-like up to 6 ML. An ab initio calculation has been performed to obtain the balance between surface and shape anisotropy energies [79]. The results indicate that the surface anisotropy, while it does favor perpendicular magnetization, is not large enough to compete
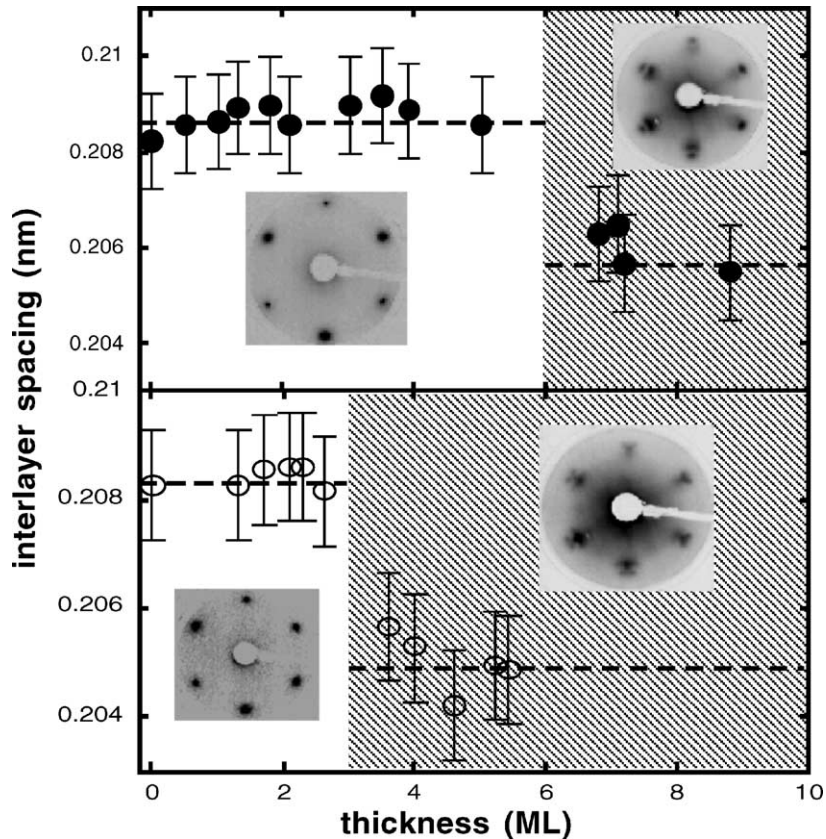
Fig. 14.   Average interlayer spacing (calculated from IV/LEED) as a function of thickness of Fe/Cu(1 1 1) films prepared by PLD (upper panel) and MBE (lower panel). The shaded area represents the thickness regime in which the bcc Fe structure has formed, as supported by both the change of interlayer spacing and the LEED patterns (inset).

against the in-plane shape anisotropy energy at thickness above 2.5 ML, in good agreement with the experimental observation.

Because of the improved morphology and structure, the PLD films are better two-dimensional ferromagnets than the MBE films by having higher magnetic stability and larger magnetic moment. The magnetic stability is characterized by the time-dependent MOKE measurements of the remanent magnetization, which is shown in Fig. 15 for the same 1.6 ML films that were imaged in Fig. 12. At the time point indicated by "field on", an external field was applied along the surface normal allowing the films to reach the saturation level quickly. After about 20 s, the external field is switched off and the remanent magnetization was monitored for a further 60 s. The remanent magnetization remains unchanged (with respect to time) only for the PLD film, indicating a high degree of magnetic stability for a perfect two-dimensional film. The MBE film, owing to its non-percolated island morphology that includes some isolated small islands, will lose part of the total magnetization (after switching off the external field) due to the spin flipping of those small islands that are not large enough to compete against the thermal fluctuation. Loosely speaking, the different time-dependent behavior in PLD and MBE films is a reflection of long versus short range order in these two types of films.
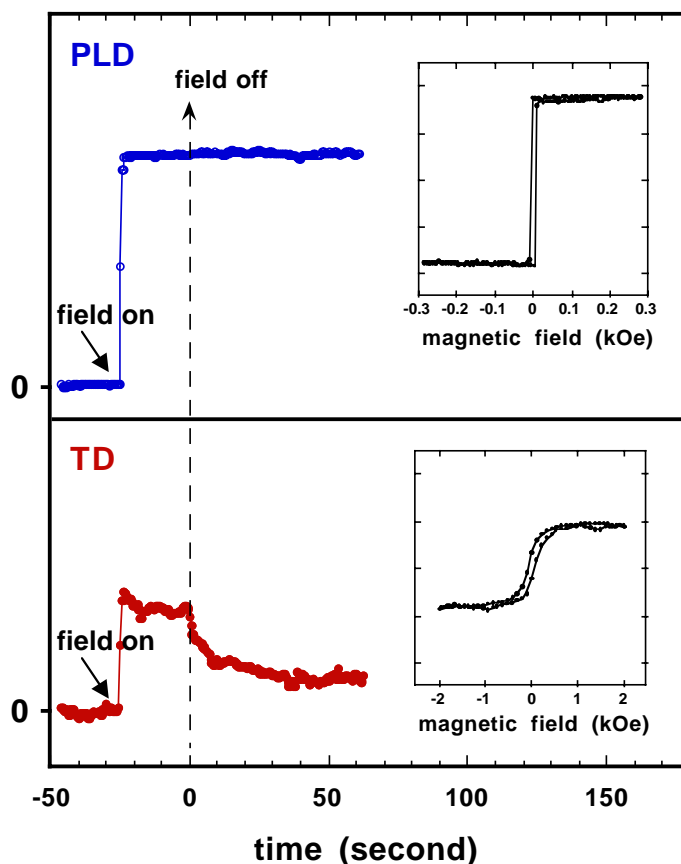
1.6 ML Fe/Cu(111)

measured at 130 K

Fig. 15. Time-dependent magnetization of 1.6 ML Fe/Cu(1 1 1) films prepared by PLD (upper) and MBE (lower). Before time point indicated by "field off" (dashed line), the films had been saturated by an external field from a demagnetizing level "0". After "field off", the magnetization of the PLD film kept constant, but the magnetization of the MBE film decayed with time.

At low thickness, the PLD films are also advantageous in terms of the size of magnetic moment. Fig. 16 shows the thickness-dependent Kerr intensity measured for PLD (filled circles) and MBE Fe/Cu(1 1 1) films (open circles). Both the MBE films and the PLD films show signs of the existence of multiple magnetic phases, as the Kerr intensities of both films do not increase with increasing thickness at a single linear slope. Assuming the MOKE intensity to be proportional to the total moment of the films, each linear slope should correspond to a magnetic phase with one particular moment, Fig. 16 then suggests that the PLD and the MBE films each have two magnetic phases. The second phase for the MBE films, based on the previously described structural studies, should have the robust magnetic moment of bcc Fe ($\sim 2.2 \mu_B$). Using the corresponding linear slope as a reference line, we can make a
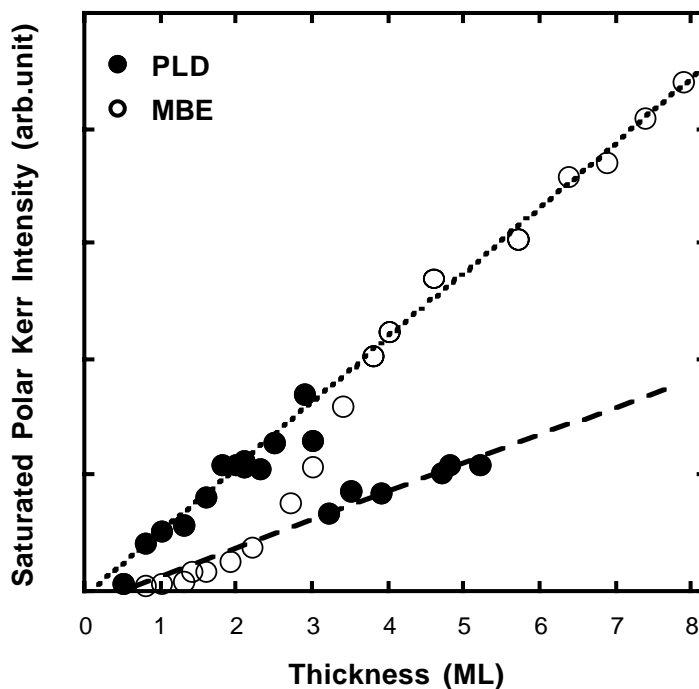
Fig. 16.   Saturation Kerr intensity as a function of thickness of Fe/Cu(1 10 1) films prepared by PLD (filled circles) and MBE (open circles). In each case a magnetic phase transition occurs, as indicated by the change of the linear increasing slope of the Kerr intensity. For MBE films, the slope, thus the magnetic moment, changes from low to high values around 3 ML. The moment of the PLD films changes in a reversed manner: high at low thickness (<3 ML), but low at high thickness (>3 ML).

rough estimation of the magnetic moment for PLD and MBE films (<3 ML) to be about 2.2 and $0.7\mu_B$, respectively. Above 3 ML, the PLD films transform into a low moment phase, possibly due to a small contraction of intra-plane lattice constant [78].

3.2. Growth and magnetism of fcc Co

In bulk, the room temperature stable hcp Co phase undergoes a hcp → fcc Martensitic phase transition at about 415 °C [80], which is considerably lower than the bcc → fcc transition temperature of Fe (914 °C). Accordingly, it is much easier to stabilize the fcc Co phase when growing thin films on a fcc substrate (e.g. Cu) at room temperature or below. Indeed, fcc Co grows layer-by-layer on a Cu(1 0 0) substrate up to at least 100 ML even with MBE [81]. The situation, however, becomes quite different for Co growth on a Cu(1 1 1) substrate, because the formation of fcc/hcp stacking faults may quicken the fcc → hcp transition. For MBE-grown Co/Cu(1 1 1) systems, the fcc/hcp stacking faults are unavoidable unless a Pb surfactant is used [82]. When grown by PLD, at low thickness the Co/Cu(1 1 1) films are stacking fault free and grow layer-by-layer. Fig. 17 shows the IV/LEED curves of (10) and (01) spots for 3 ML PLD and MBE-grown Co/Cu(1 1 1) films. The MBE-grown film has a six-fold symmetry in the LEED pattern corresponding to that of the hcp structure. The PLD film has the same three-fold symmetry as that of the Cu(1 1 1) substrate, and thus is in epitaxial fcc(1 1 1) phase.
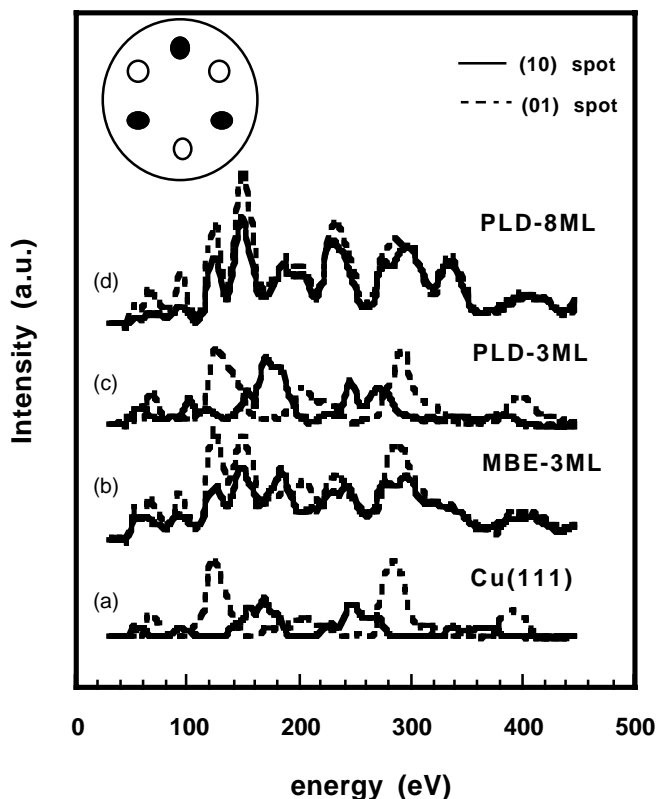
Fig. 17. LEED intensity vs. energy (*I–V*) curves for the (10) and (01) beams of (a) clean Cu(1 1 1), (b) 3 ML TD-Co/Cu(1 1 1) films, (c) 3 ML PLD-Co/Cu(1 1 1) films, and (d) 8 ML PLD-Co/Cu(1 1 1). The similarity of curves (a) and (c) indicates hcp structure is suppressed in PLD films.

By calculating the thickness-dependent interlayer distance (Fig. 18), we conclude that the MBE and the PLD grown Co/Cu(1 1 1) films transform into the hcp phase at ∼3.5 and ∼6.5 ML, respectively. Moreover, as shown in Fig. 19, even in high thickness regime where both types of films are in the hcp structure, the PLD films remain much smoother than the MBE films.

The different fcc → hcp transition process results in different magnetic behavior in the MBE and the PLD grown Co/Cu(1 1 1) films. Fig. 20 shows magnetic hysteresis loops recorded with field along the in-plane (left) and perpendicular (right) directions for MBE and PLD grown films. MBE films have an in-plane easy magnetization axis at thicknesses below 6 ML. As soon as the thickness exceeds 6 ML, the films have both perpendicular and in-plane components as evidenced by the finite remanent magnetization along the two directions. The perpendicular components at high thickness may come from some of the hcp Co islands with a relatively large height but small lateral dimensions. These islands tend to have a large uniaxial magnetocrystalline anisotropy along the *c*-axis, i.e. the direction perpendicular to the film plane, but a reduced in-plane shape anisotropy due to the enhanced aspect ratio. Such islands, however, do not exist in the PLD films either before or after the fcc → hcp transition, which explains why the PLD films have an in-plane easy magnetization axis throughout the whole film thickness range studied.
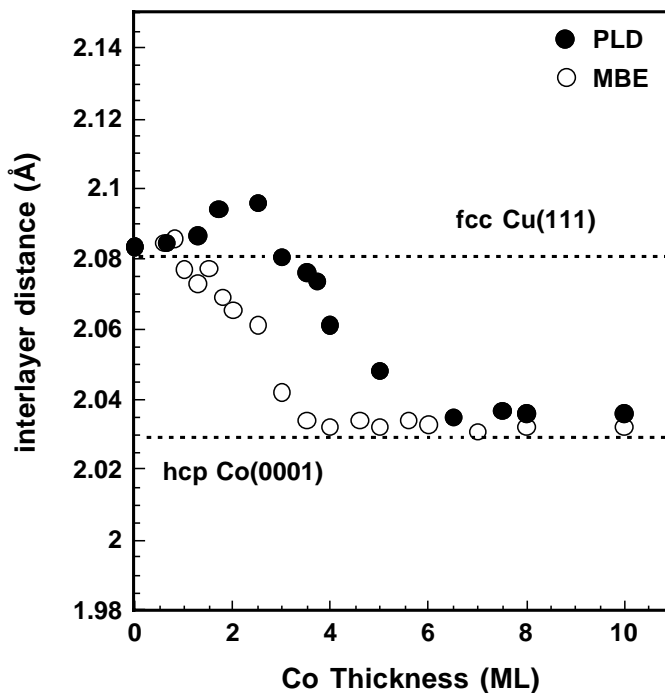
Fig. 18.   Average interlayer spacing (calculated from IV/LEED) as a function of thickness of Co/Cu(1 1 1) films prepared by PLD (filled circles) and MBE (open circles). The dashed lines indicate the interlayer distances of fcc Cu(1 1 1) and hcp Co(0 0 0 1) in bulk. The fcc → hcp transition occurs at higher thickness in the PLD films.
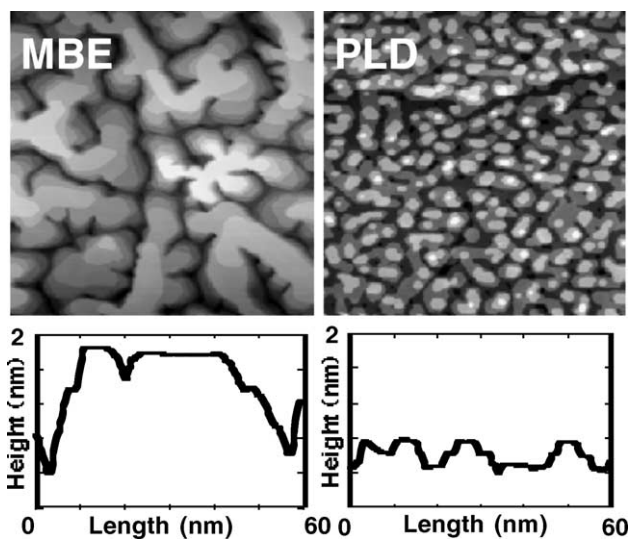

Fig. 19.   STM topography images of 7.9 ML Co/Cu(1 1 1) films grown by MBE (left) and PLD (right). The corresponding line profiles show that the MBE film has a four-times higher peak-to-peak roughness.
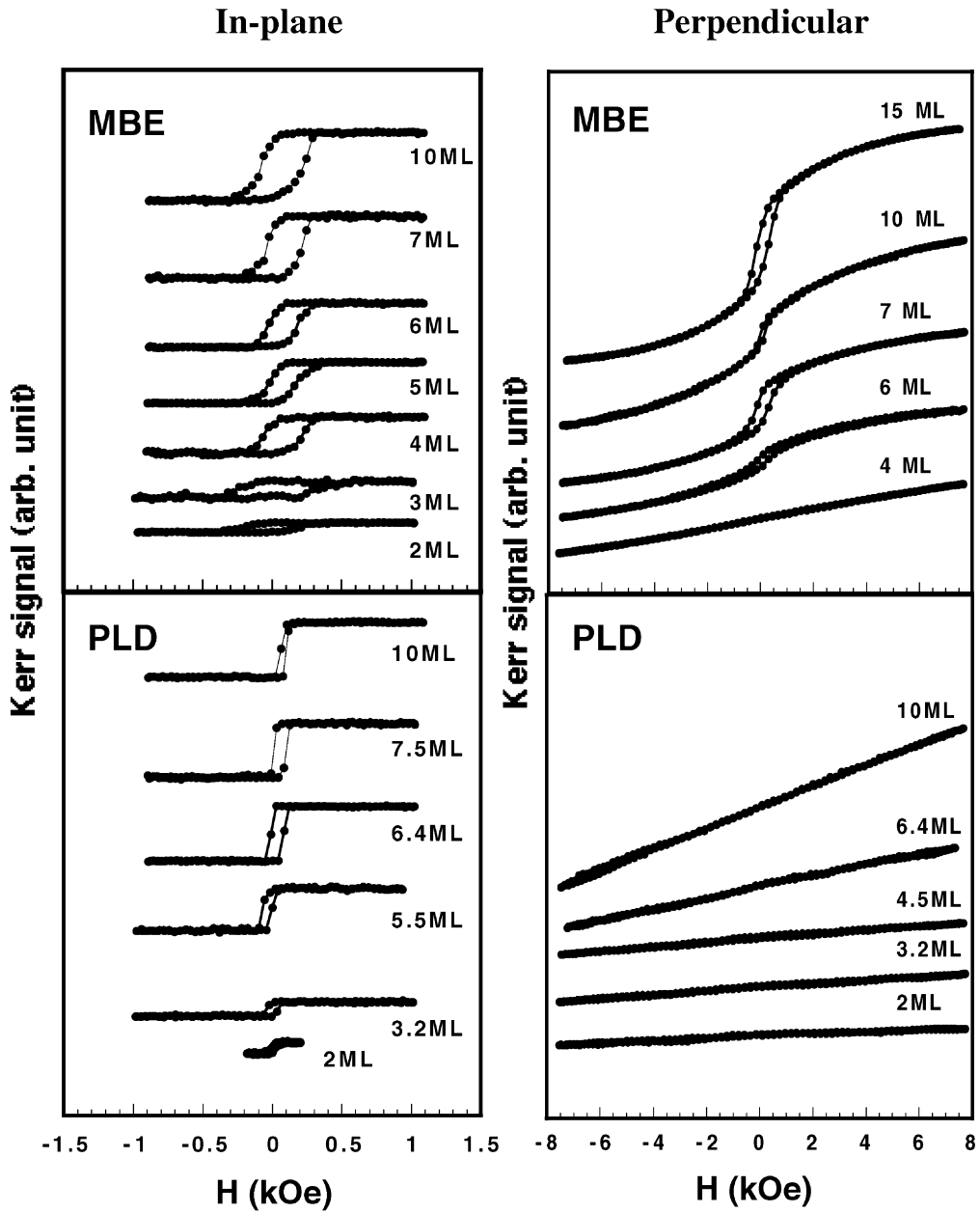
Fig. 20. In-plane and perpendicular Kerr hysteresis loops of MBE and PLD grown Co/Cu(1 1 1) films. The PLD films have an in-plane easy magnetization axis at all thicknesses studied. The MBE films are in-plane magnetized below 6 ML, and start to show both in-plane and perpendicular components above 6 ML.

3.3. Artificial layered alloys

Having shown the stabilization of fcc Fe and fcc Co phases in ultrathin films by PLD, we now introduce a new class of metastable materials, namely a special type of binary alloy that is fabricated by monatomically stacking two different kinds of metallic materials. When this approach was first introduced by Takanashi et al. [83], it was used to grow FeAu $L1_0$ alloy by means of conventional MBE growth. Later on, several other kinds of ordered binary alloys, including CoRu [84], AuCu [85], and AuNi [86] monoatomic superlattices, have been formed using MBE growth. These artificial ordered alloys, though not attainable in bulk form, all display remarkable stability in thin film form possibly due to the kinetic limitations and epitaxial stress associated with thin film growth. These nanostructured materials constructed with atomic-scale precision can have intriguing magnetic properties [83,87], which can be exploited in potential technological applications.

Because PLD tends to improve the two-dimensional growth, which is an essential prerequisite to fabricate such monatomic superlattices, PLD should be the method of choice to grow high-quality monatomic superlattices. This is particularly true if one would like to use monolayer fcc-like Fe as one of the constituents, since it can not be grown by MBE on both Cu(1 0 0) and Cu(1 1 1) substrates. In the following, we will introduce the growth and magnetic properties of two artificial alloys, FeCu $L1_0$ and FeCo $L1_0$ structures. The two alloys have opposite bulk miscibility—Fe and Cu are immiscible, but Fe and Co have solid solutions at all concentration. Interestingly, the structural stability of these two alloys is dramatically different, which reveals some very interesting physics as the underlying mechanism.

3.3.1. Fe/Cu $L1_0$ alloy

In equilibrium, Fe and Cu have very little mutual solid solubility and form no intermetallic compounds, even though their atomic radii are quite similar. This behavior is in accordance with the positive value of the calculated heat of mixing between Fe and Cu. By using vapor-quenching methods [88,89] or high-energy ball milling [90–92], the solid miscibility can be extended, and a metastable FeCu solid solution can be formed over the entire range of composition. In contrast to the above-mentioned techniques which produce *polycrystalline* or *amorphous* metastable alloys, a single crystalline ordered alloy can be grown by means of epitaxially stacking monolayers of Fe and Cu alternately onto an appropriate substrate. If this substrate is Cu(1 0 0), then the formed alloy is of $L1_0$ type. Due to the small lattice mismatch between fcc Fe and fcc Cu (~1%), one would expect a lasting layer-by-layer growth for this [1 ML Fe/1 ML Cu]$_n$ superlattice. However, some kind of structural transition may eventually occur because of the metastability of such $L1_0$ Fe/Cu alloy.

The growth of each monolayer of Fe and Cu by PLD was monitored by in situ RHEED. Fig. 21 shows typical RHEED oscillations for a 6 ML ($n = 3$) Fe–Cu stacking grown on Cu(1 0 0) at room temperature. The first maximum corresponds to 1 ML Fe and the second maximum corresponds to the second layer completion by 1 ML Cu. The RHEED oscillations decay with increasing thickness and finally disappear when the total thickness approaches 44 ML. In situ STM and LEED studies revealed that the disappearance of RHEED oscillations coincides with the fcc to bcc structural transition. Fig. 22 shows a few snap shots of the surface morphology obtained by STM during film growth. At low thickness (<44 ML), the FeCu alloy films show good layer-by-layer morphology. At higher thickness, the films become very rough with ⟨1 1 0⟩ oriented ridges that have a similar morphological appearance to that of the bcc Fe films on Cu(1 0 0) [93]. The RMS surface roughness during the monolayer stacking is shown as a function of the total number of monolayers of [1 ML Fe/1 ML Cu]$_n$ in Fig. 23.
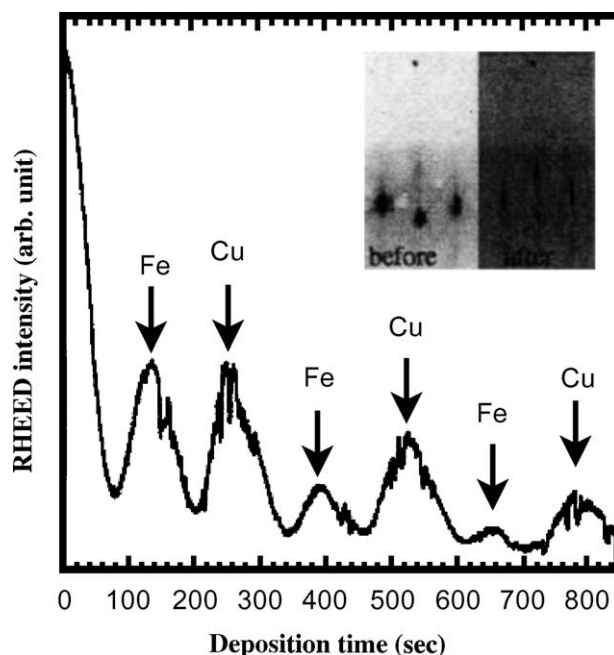
Fig. 21. Typical RHEED oscillations for a 6 ML Fe–Cu monoatomic stacking on Cu(1 0 0) prepared by PLD. The first maximum corresponds to 1 ML filling of Fe and the second maximum corresponds to an addition of 1 ML Cu, and so forth. Inset: RHEED pattern before and after deposition.

The roughness tends to increase between 2 and 10 ML and then fluctuates around an average value of 0.14 nm. This trend in roughness is consistent with the observed nearly layer-by-layer growth of the FeCu films, which involves a maximum of three monatomic levels at any time. Between 40 and 50 ML, the roughness shows a big jump from 0.15 to over 0.3 nm. Correspondingly, LEED patterns (Fig. 24) indicate that the films are in fcc (1×1) structure before the transition, and become bcc-like with a "3×1"-like pattern. The latter was also observed in the bcc Fe films on Cu(1 0 0) as a characteristic feature for a Pitsch orientation [94].

While the $L1_0$ FeCu alloy is a metastable phase, the fcc $\rightarrow$ bcc structural transition is likely associated with the surface roughening process. With increasing thickness, the increased roughness means the enhanced probability for neighboring Fe layers to make direct contact at some locations. If at certain locations the directly contacted Fe layers exceed 4 or 5 ML thickness, they may initiate a local fcc to bcc transition in the same manner as what occurs in the pure Fe films on Cu(1 0 0). This picture is also backed by the observation that the LEED patterns and STM morphology recorded from the transformed bcc films of the FeCu superlattice and the pure Fe on Cu(1 0 0) are almost identical.

The magnetic properties of the $L1_0$ FeCu alloy are of great interest, not only because it is a new magnetic material that has not been investigated, but also because the possible induced magnetic moment in Cu which can affect the coupling between the Fe layers. In situ MOKE measurements attest that the thin films of the $L1_0$ FeCu alloy have an in-plane easy magnetization axis for all film thickness, which include the low thickness limit of 2 ML (one unit cell along growth direction). Note that an uncovered 1 ML Fe film on Cu(1 0 0) is perpendicularly magnetized, but switches the magnetization to
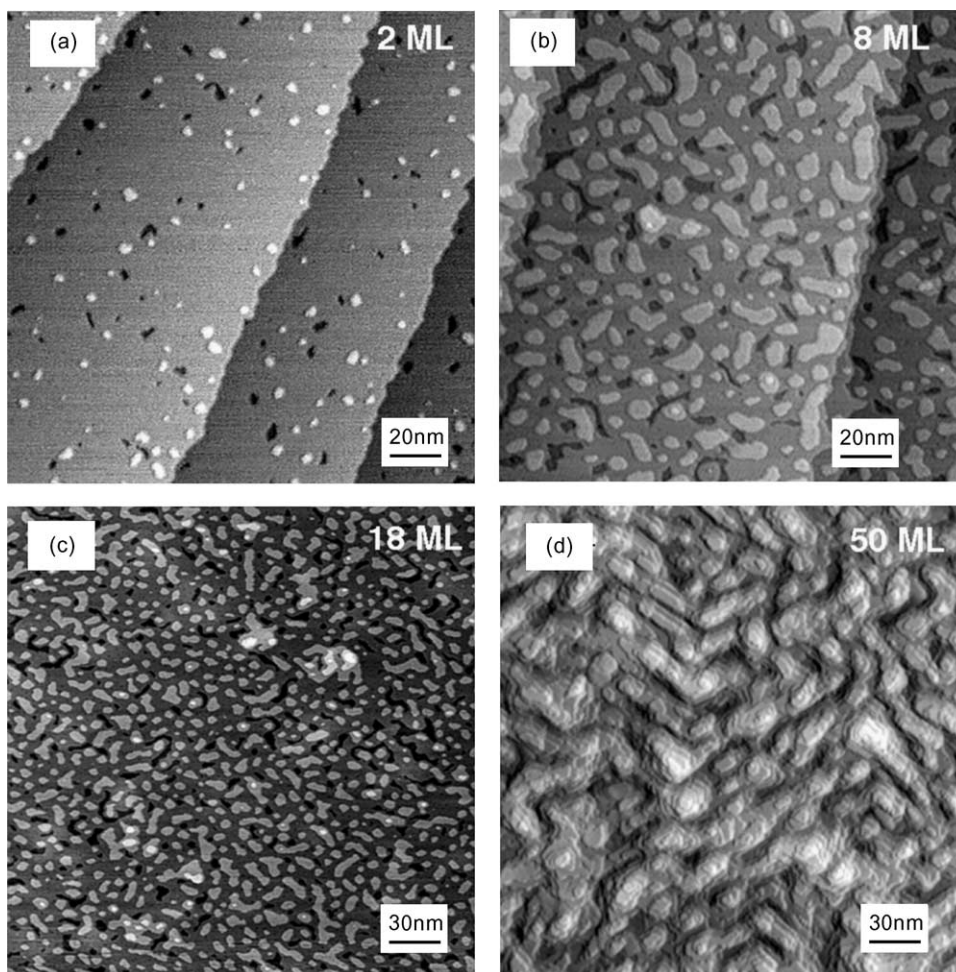
Fig. 22. Surface topography of $L1_0$ Fe/Cu alloy deposited on Cu(1 0 0) by PLD at room temperature: (a) 2 ML, (b) 8 ML, (c) 18 ML, and (d) 50 ML. Note that the 50 ML film changes to a ridge-like morphology with two 90° oriented domains.

the in-plane direction once a monolayer of Cu is capped on top. Typical magnetic hysteresis loops of these films are shown in Fig. 25 for a 6 ML film in (a) and a 20 ML film in (b).

The saturation magnetization and Curie temperature of the $L1_0$ FeCu films are shown in Fig. 26 as a function of film thickness. The saturation magnetization increases linearly with increasing thickness, indicating that the films are in a uniformly magnetized ferromagnetic phase. The Curie temperature, after an initial increase, reaches a saturation of about 400 K when thickness exceeds 8 ML. This saturation is likely not induced by Fe–Cu interdiffusion because the magnetic measurements are reversible after another cooling–heating cycle [95]. Therefore, one may conclude that the Curie temperature for this new magnetic material, i.e. $L1_0$ FeCu, is about 400 K.

Spin-resolved electronic structure and element-resolved magnetic properties of the $L1_0$ FeCu alloy films have been investigated by spin-resolved valence-band photoemission and soft X-ray magnetic circular dichroism (XMCD) [96]. The photoemission results again confirmed the $L1_0$ order in the FeCu
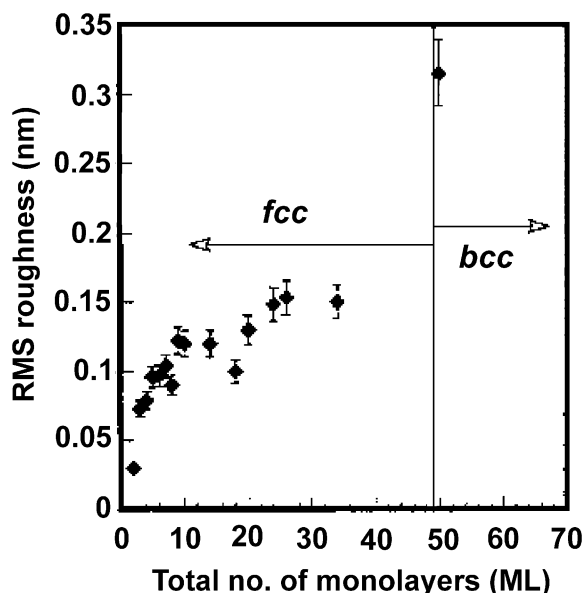
Fig. 23. Plots of root mean square (RMS) roughness vs. thickness as measured by STM. After an initial increase, the RMS seems to approach an average of 0.14 nm in the fcc $L1_0$ regime, but increases by more than a factor of two when the films become bcc-like (>50 ML).

monatomic superlattices. The magnetic moment of both Fe and Cu were determined by XMCD spectra recorded at Fe $L_{2,3}$ and Cu $L_{2,3}$ edges, respectively. The spin moment, orbital moment and the ratio between the spin and orbital moments are summarized in Table 1 for two $L1_0$ FeCu films in comparison with the data from the Fe/Co, Co/Cu and Fe/Cu multilayers. For the $L1_0$ FeCu, the Fe orbital moments were found to be strongly enhanced in FeCu with respect to pure Fe. The induced Cu d moments amount to about $0.11\mu_B$, which is attributed to the electronic hybridization between Fe- and Cu-derived states and reduced dimensionality of the alloy films [96].

3.3.2. Fe/Co $L1_0$ alloy

In the bulk phase diagram a stable bcc alloy, Fe_xCo_{1-x}, exists for a range of concentration, $0.3 \leq x \leq 0.75$, and is denoted as α'. Samples with $x = 0.5$ which are annealed sufficiently slowly form an ordered structure, equivalent to that of cesium chloride, known as the B2 phase. It is noteworthy both for its unusually high magnetic moment and for its high Curie temperature. The extrapolated Curie temperature from magnetization versus temperature measurements is >1500 K, higher than any other known magnetic material [97].

With the same approach we described to grow the $L1_0$ FeCu alloy, one should be able to use PLD to obtain the $L1_0$ ordered phase of FeCo alloy on Cu(1 0 0). Interestingly, the $L1_0$ phase and the B2 phase differs only in their *c/a* ratios (1.0 and 0.71, respectively), giving a possibility for a potential structural transition from the metastable $L1_0$ phase to the stable B2 phase. This transition, based on conventional epitaxial stress arguments, should not occur at low film thickness because the $L1_0$ FeCo structure has a much smaller lattice mismatch (∼1%) than that of the B2 FeCo structure (∼13%) when grown on Cu(1 0 0) substrate.
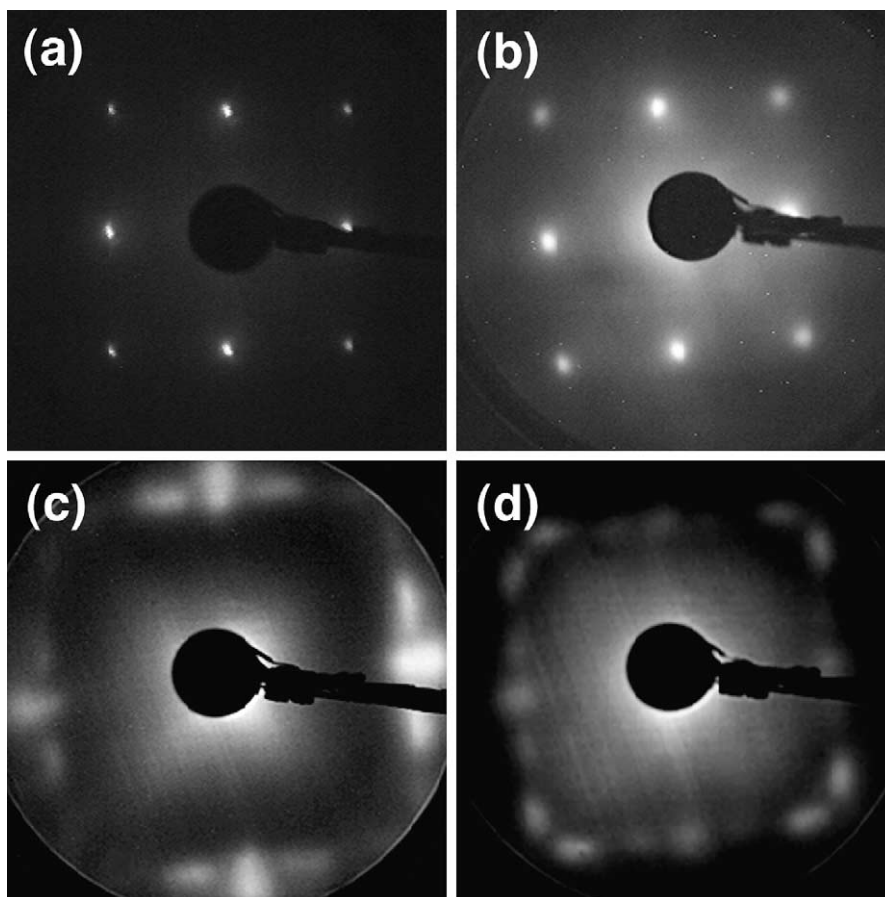
Fig. 24. LEED patterns of a (a) clean Cu(0 0 1) at 156 eV showing a $p(1 \times 1)$ structure, (b) 44 ML $L1_0$ FeCu still showing $p(1 \times 1)$ fcc structure, and (c) and (d) 50 ML FeCu showing a "3×1"-like pattern which is characteristic for a pitch orientation of a bcc(1 1 0) lattice on an fcc(1 0 0) lattice at 68.5 and 90 eV, respectively.

The experimental observation was totally surprising. It was found that the FeCo $L1_0$ phase can be grown only up to three unit cells (6 ML in total) on Cu(1 0 0) [98]. Fig. 27 shows (a) the RHEED intensity, (b) STM calibrated surface RMS roughness, and (c) magnetic coercivity (at room temperature) and Curie temperature as a function of the film thickness. All data indicate that the growth of the FeCo $L1_0$ alloy can be divided into two regimes. In regime I (below and up to 6 ML of total thickness), the 1 ML Fe/1 ML Co films grow layer-by-layer as indicated by the RHEED oscillations. Sharp (1×1) LEED spots were observed for all film thickness within this regime (inset). In regime II (beyond 6 ML of total thickness), LEED could only detect a high background intensity without any clearly visible diffraction spots. The films become rougher as evidenced by the gradual disappearance of RHEED oscillations and sharp increase of the RMS roughness. MOKE measurements (Fig. 27(c)) show increased coercivity due to surface roughening above 6 ML. The Curie temperature (Fig. 27(c)), while already leveling out at 250 °C for 4 and 6 ML films (regime I), shoots up well beyond 350 °C (maximum measuring temperature) for a 8 ML film (regime II). The definition or division of the two
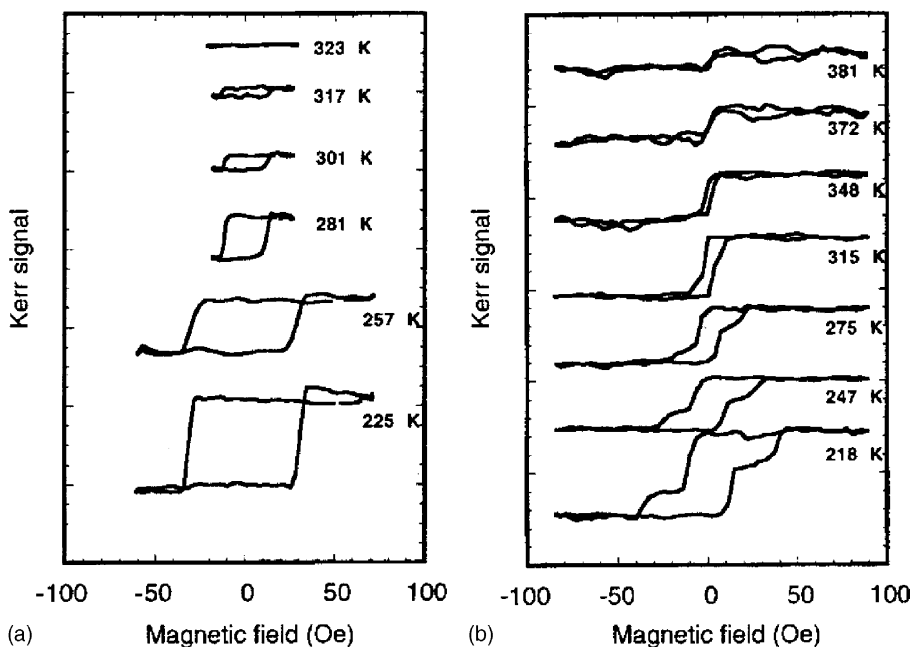
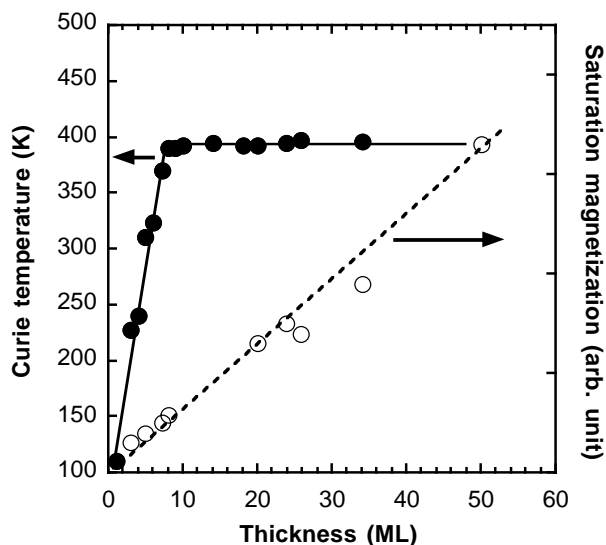Fig. 25. In-plane MOKE hysteresis loops of a (a) 6 ML and (b) 20 ML L1$_0$ FeCu films prepared by PLD.

Fig. 26. Curie temperature (filled circles) and saturation magnetization (open circles) vs. thickness of L1$_0$ FeCu films prepared by PLD. The saturation magnetization increases linearly with thickness, as expected from a uniformly magnetized system. The Curie temperature reaches a saturation level of 400 K beyond 8 ML.

Table 1

Spin (μ_S) and orbital (μ_L) magnetic moment of Fe and Cu atoms in PLD-grown $L1_0$ FeCu on Cu(1 0 0) from a sum-rule analysis of XMCD measurements, as well as their ratio μ_L/μ_S[a]

Sample	Atom	μ_S (μ_B)	μ_L (μ_B)	μ_L/μ_S
10 ML FeCu	Fe	1.8	0.21(5)	0.12(3)
	Cu	0.05	0.006(3)	0.12(6)
	Cu (film only)[b]	0.12	0.014(7)	0.12(6)
22 ML FeCu	Fe	1.8	0.26(6)	0.13(3)
	Cu	0.08	0.004(2)	0.05(3)
	Cu (film only)[b]	0.11	0.005(3)	0.05(3)
3.5 ML Fe/5 ML Co	Fe	1.9	0.08(2)	0.04
20 nm $Co_{90}Cu_{10}$[c]	Cu	0.114[c]	0.009[c]	0.08[c]
[1 nm Fe/0.3 nm Cu]$_{20}$[c]	Cu	0.078[c]	0.007[c]	0.09[c]

[a] For comparison the result of a 3.5 ML Fe film on 5 ML Co/Cu(1 0 0), and literature values (G.A. Held, et al., Z. Phys. B 100 (1996) 335) for a random Co90Cu10 alloy and an Fe/Cu multilayer are also listed.

[b] Corrected to exclude the Cu substrate contribution, assuming an electron mean free escape depth of 11 ML ($\sim$2 nm).

[c] From G.A. Held, et al., Z. Phys. B 100 (1996) 335.

growth regimes does not change if the growth is begun with either Fe or Co showing minimum effect of the substrate on the structural transition.

Direct evidence that the $L1_0$ structure forms only in regime I is provided by X-ray diffraction. To enhance the contrast, the X-ray energy was set just below the Co edge (7705 eV). Fig. 28 shows the X-ray reflectivity from a sample with three unit cells of FeCo (six ML total). The dominant features are the diffraction from bulk copper at momentum transfer $L = 0, 2$. The next largest feature, at $L = 1.5$ can be identified with the (1 1 1) planes of Cu_2O (lattice constant of 4.258 Å) which was formed on the Cu cap during transport of the sample. More interesting for this study is the diffraction intensity near $L = 1$. This peak is clearly associated with the FeCo layers, since it is not observed for X-ray energies away from the Co edge (specifically, at 7500 and 8500 eV). Its location at half the distance of the bulk Cu peak in reciprocal space indicates a doubling of the real space lattice, precisely that expected for an $L1_0$ structure. In regime II, the $L1_0$ order is destroyed by the abrupt roughening process above 6 ML. Consequently, no X-ray diffraction was observed at $L = 1$.

The unexpected quick collapse of the $L1_0$ FeCo alloy, as revealed by first-principles calculations, is caused by an $L1_0 \rightarrow B2$ structural phase transition that is associated with the relative electronic stability of the two alloy phases in reduced dimensionality. Fig. 29 shows the total energy of bulk and thin FeCo monatomic slabs in the ordered face-centered-tetragonal (fct) structure as a function of the c/a ratio. Note that the c/a ratios for the $L1_0$ structure and the B2 structure equal 1 and 0.707, respectively. For bulk FeCo, although the total energy is minimized at $c/a = 0.707$, there is a 'shoulder' in the energy versus c/a curve near $c/a = 1.0$. Such a 'shoulder' indicates that a structural transformation is possible when atoms are in a different environment than in the bulk. Indeed, this "shoulder" is developed into a true energy minimum for thin FeCo slabs. For the seven-layer slabs, a local energy minimum is developed near $c/a = 1.0$, however, the slab maintains the absolute energy minimum at the c/a ratio close to that of the bulk B2 structure. For the five-layer slabs, the system stabilizes near the $c/a = 1.0$ region, whereas the minimum corresponding to the B2 structure begins to disappear; for the three-layer slabs, the slab is stabilized near $c/a = 1.05-1.10$, whereas the structure
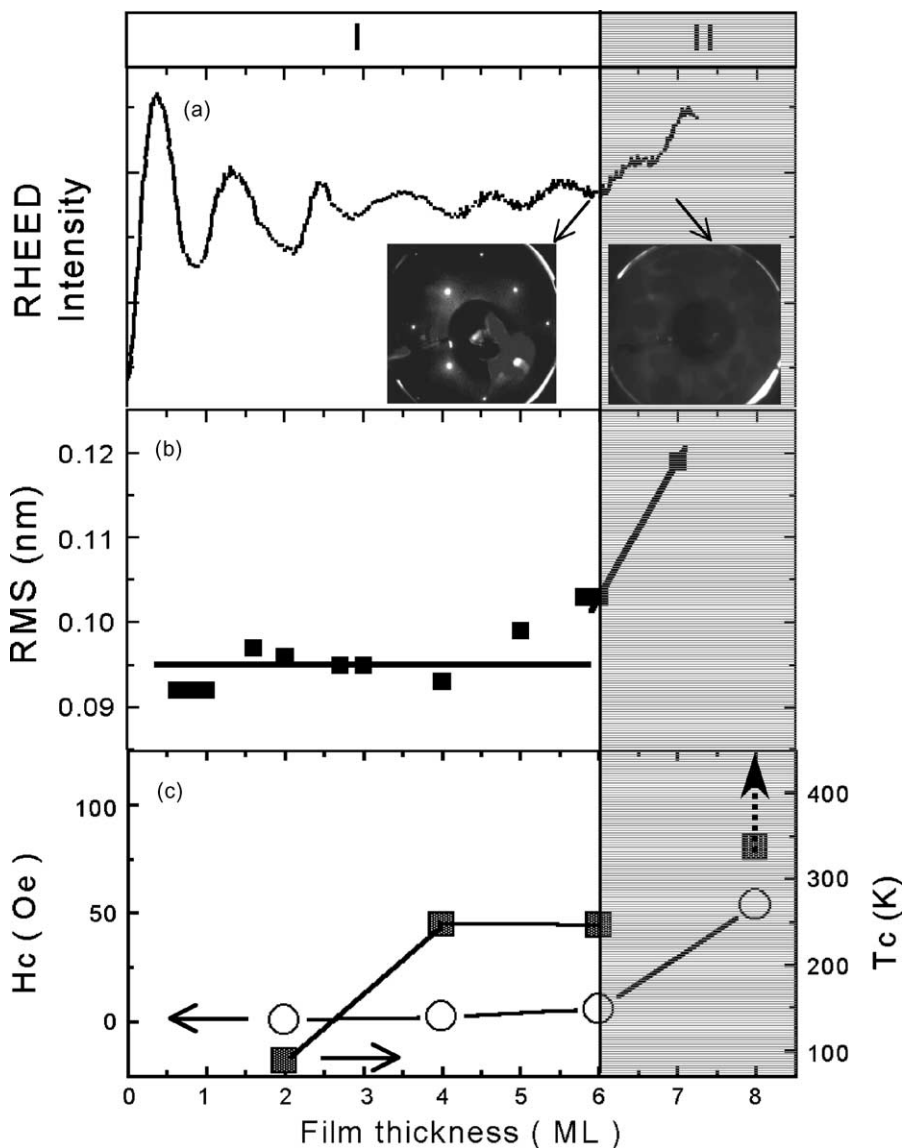
Fig. 27. RHEED intensity (a), STM calibrated surface RMS roughness (b), and magnetic coercivity (open circles) and Curie temperature (filled squares) (c) as a function of the Fe/Co film thickness. In growth regime I, films grow layer-by-layer, and in regime II, significant surface roughening occurs. The insets in (a) are the corresponding LEED patterns (142 eV) of the two growth regimes.

near $c/a = 0.707$ becomes unstable. Therefore, the effect of the reduced dimensionality is to induce a structural change in the Fe/Co slabs, from the B2 structure (for seven or more atomic layers) to the $L1_0$ structure (for five or less atomic layers).

These calculated results provide a clear picture for the experimental observations. At low thickness, the system prefers, energetically, to be in $L1_0$ structure, which has a lattice constant (3.58 Å for
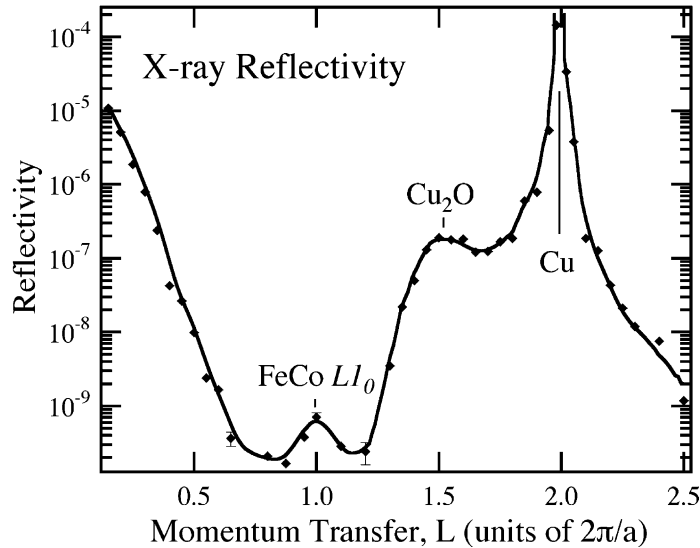
Fig. 28.   Ex situ X-ray reflectivity from a three bilayer film of FeCo capped with Cu. Diffraction peaks from the Cu substrate, a surface Cu-oxide, and the FeCo film are observed. Diffraction intensity and location are consistent with an $L1_0$ structure with little intermixing.

$c/a = 1.0$) sufficiently close to that of Cu (3.61 Å) allowing a good layer-by-layer growth. At higher thickness, the system can minimize its energy by transforming into the more stable B2 phase. However, because the B2 structure has a large lattice mismatch with Cu ($\sim$12%), layer-by-layer growth breaks down and a significant surface roughening is thus observed experimentally. Note that the structural change occurs for the slab thickness between five and seven layers, which agrees well with experimental findings of 6 ML.

Band structure calculations also revealed the electronic origin of this thickness-driven structural phase transformation. In the Fe/Co slabs, the majority-spin states are nearly fully occupied, therefore, our discussions below are focused on the minority-spin channel, which determines the structural stability of thin Fe/Co slabs. The electronic structure of bulk B2 FeCo is characterized by the presence of a pseudo-gap separating the bonding and non-bonding states. In Fig. 30 we show the layer-projected electron density-of-states (DOS) of the Fe-terminated seven-layer slab with the B2 structure. For the bulk-like Fe atoms, the Fermi level (E_F) is located near the valley of the pseudo-gap. On the other hand, for the surface Fe atoms, the band narrowing smears out the pseudo-gap in the local DOS profile, resulting in a high DOS at E_F ($N(E_F)$). The surface atoms therefore exhibit slightly enhanced magnetic moments but have much higher $N(E_F)$ than the bulk-like atoms. Therefore, the structural stability of the B2 Fe/Co slabs will depend on the surface-to-bulk volume ratio. From our calculations for layer thickness less than or equal to five layers, the B2 structure becomes unstable. By contrast, in the close-packed $L1_0$ structure (with $c/a \sim 1$), the separation between the bonding and non-bonding states in the DOS profile is less well-defined than that of the open B2 structure, because the electronic interaction in the $L1_0$ structure is no longer dominated by the nearest-neighbor interaction as in the B2 structure. An examination on the layer-projected DOS of the seven-layer slab with the $L1_0$ structure shows that, while the band narrowing is still present at the surface, the change of $N(E_F)$ from the center layer to the surface layer is insignificant. In other words, although the bulk FeCo is stabilized in the B2 structure, it
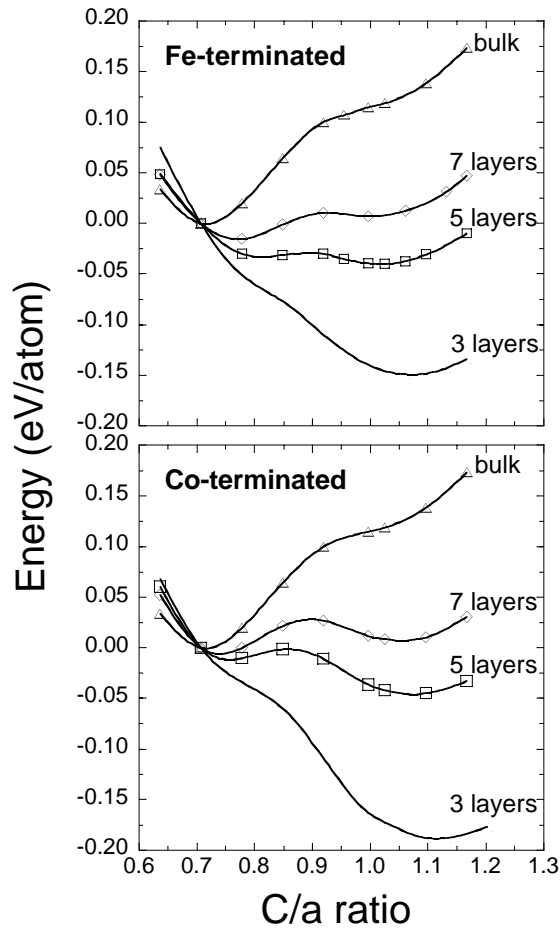
Fig. 29.   The total energy of Fe-terminated (top) and Co-terminated (bottom) slabs as a function of *c/a* ratio. The energy of the B2 structure is set as the reference in each case (i.e. as zero energy).

is far more costly in energy to create a surface on the B2 lattice than on the L1$_0$ lattice. As a result, the L1$_0$ structure becomes lower in energy than the B2 structure as the number of layers in the slabs decreases, i.e. the "shoulder" in the energy versus *c/a* curve for the bulk becomes the true energy minimum for slab thickness below five layers. We note that, though the calculation is performed on free-standing Fe/Co slabs, the overall mechanism presented here is expected to be valid even in the presence of the Cu(0 0 1) substrate, since the electronic d-states of Fe/Co near E_F are hardly affected by Cu due to clear separation between their d-bands.

4. Magnetic multilayers by PLD

Compared with techniques such as sputter deposition and MBE, the application of PLD in growing magnetic multilayers is relatively limited [99,100] possibly due to concerns of droplet formation and
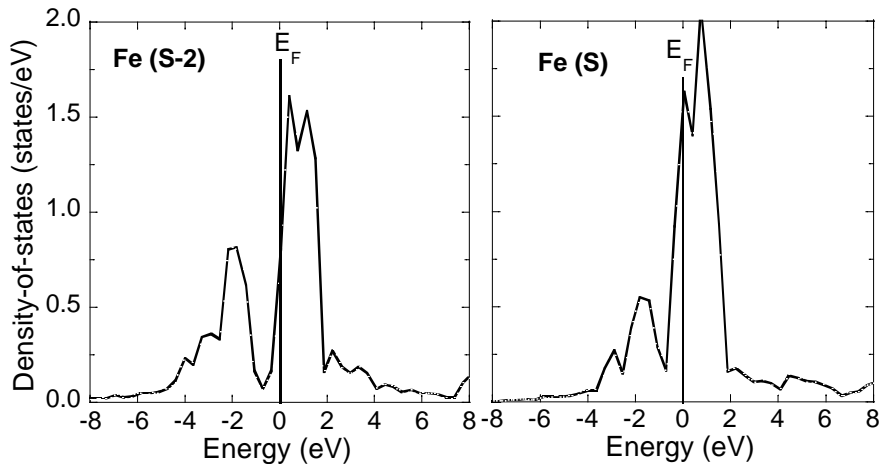
Fig. 30. The layer-projected minority-spin density-of-states for the Fe-terminated seven-layer slab with B2 structure. For comparison, only those of the inner (S-2) (left) and surface (S) (right) Fe layers are shown.

high-energy ions induced interfacial roughness. These problems, however, can be largely removed by properly controlling the laser fluence as well as the substrate–target distance. In fact, as we will show below in Section 4.1, it can be advantageous to use PLD in order to obtain desired interfaces in magnetic multilayers. In addition, PLD has several other advantages that include the convenient tuning of both the deposition rate and the thickness by controlling the laser repetition rate and the number of laser pulses, respectively, and relatively easy growth of multilayers that involve refractory elements [101,102], which are generally very hard to vaporize. So far, even with the limited work of PLD growth of magnetic multilayers, some very interesting results have been obtained in the study of giant magnetoresistance (GMR) and magneto-optical recording.

4.1. Interlayer exchange coupling and giant magnetoresistance

Ever since the first observations of the GMR effect in a Fe/Cr metallic multilayer system [103,104], researches on GMR multilayers and related issues soon have become the frontier in the field of magnetism. In order to have a large GMR effect, searching for the best combination of ferromagnetic and non-magnetic materials to form multilayers is the most essential part of the effort. Of all the candidate material combinations, Co/Cu has received a lot of attention because of the large difference of the scattering rate for Co majority and minority electrons at the Co/Cu interfaces. This difference is primarily caused by the large potential mismatch between the minority electronic states of Co and Cu. In addition, Butler et al. have shown that electron channeling can significantly affect the GMR effect provided the Co/Cu interfaces are atomically smooth [105].

Having sharp interfaces in GMR multilayers is also essential to avoid any possible short circuits between the adjacent ferromagnetic layers. The occurrence of short circuits will decrease the antiferromagnetic coupling between the ferromagnetic layers and thus the GMR effect. It is therefore desirable to grow the multilayers in a layer-by-layer mode with minimum intermixing at the interfaces. In previous sections we have already shown that PLD is a suitable technique for layer-by-layer growth, although the high kinetic energy may induce some degree of intermixing at the interfaces. The

intermixing, however, can be suppressed by increasing the target-to-substrate distance, as demonstrated by a recent conversion electron Mössbauer spectroscopy study from Fe/Ag multilayers [106]. In the case of growing (1 1 1)-oriented Co/Cu multilayers, we have shown in Section 3.2 that PLD works very well to grow single layers of Co on Cu. Here we show that PLD is also suitable to grow high-quality Co/Cu/Co trilayers, which indeed exhibit the preferred antiferromagnetic coupling between the two Co layers.

Fig. 31 shows side-by-side comparison of STM images recorded from 4 ML Co/4 ML Cu/4 ML Co trilayers on Cu(1 1 1) that were grown by MBE (left) and PLD (right). In the sequence of the MBE
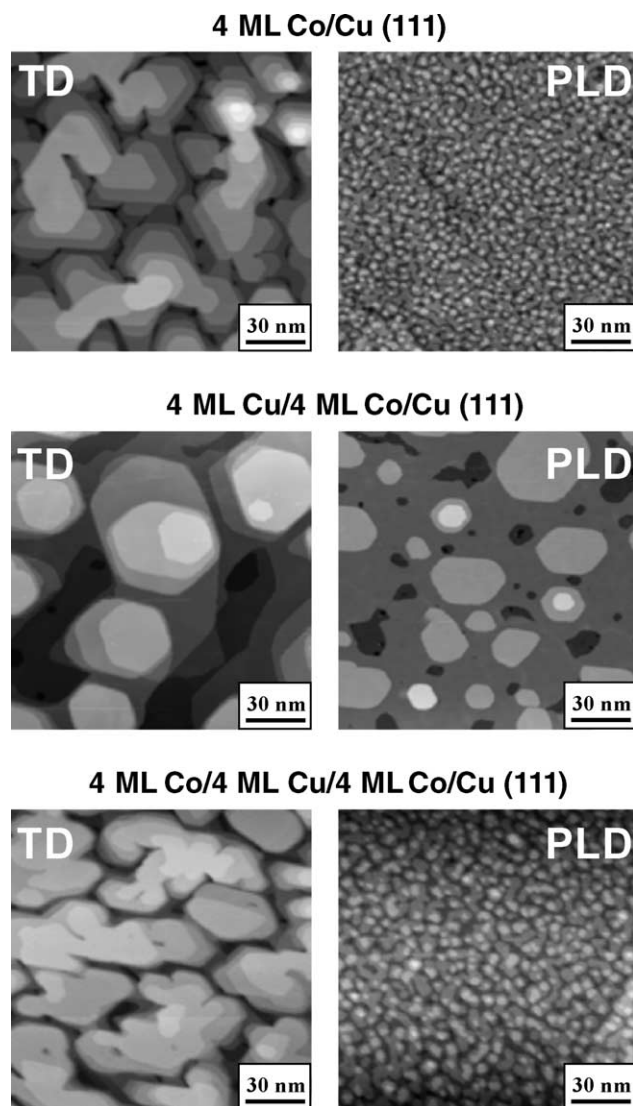

Fig. 31. STM snap shots of the growth of 4 ML Co/4 ML Cu/4 ML Co trilayers on Cu(1 1 1) by MBE (left column) and PLD (right column). The roughness in the MBE film is such that the two adjacent Co layers are partially in direct touch. The PLD film has no such short circuits due to a layer-by-layer growth.
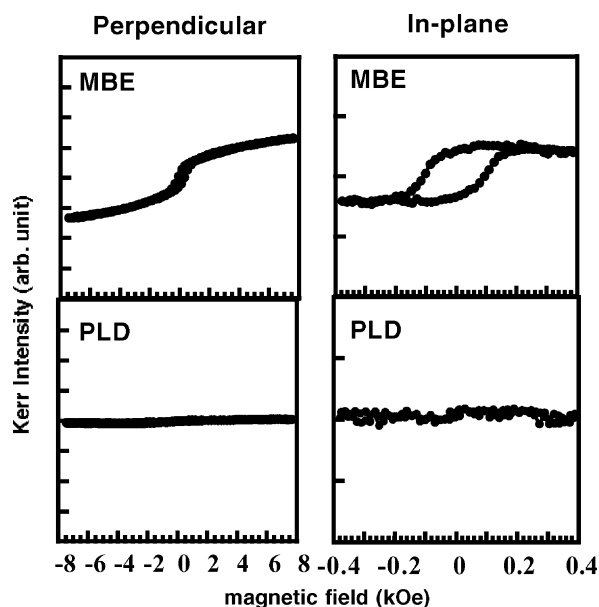
Fig. 32.   Perpendicular and in-plane Kerr loops of the Co/Cu/Co trilayers shown in Fig. 31. Complete antiferromagnetic coupling between the two Co layers has been achieved in the PLD film, as no net magnetization can be detected. The finite remanent magnetization in both perpendicular and in-plane directions of the MBE film indicates partial ferromagnetic coupling due to the short circuits between the two Co layers.

growth, the first 4 ML Co was grown with high roughness and fcc–hcp stacking faults, which significantly hinder the smooth growth of Cu layers. As a result, after the growth of 4 ML Cu, many areas of the films are still exposed to the surfaces of the bottom Co layers. Capping the film with another 4 ML Co will only lead to many short circuits between the two Co layers. This severe problem is totally removed in the PLD growth, because the film grows in a nearly ideal layer-by-layer manner for both Co and Cu. Therefore, the PLD forms a high-quality trilayer with atomically smooth Co/Cu interfaces.

In the corresponding MOKE measurements, as shown in Fig. 32, the MBE-grown trilayer had finite remanent magnetization along both perpendicular and in-plane directions. This is consistent with the magnetic properties of single-layer MBE-grown Co/Cu(1 1 1) films, which have magnetization components in the two orthogonal directions due to the coexistence of fcc and hcp multilayers islands. The finite remanence also indicates that the two Co layers are at least partially ferromagnetically coupled, otherwise the system should exhibit zero remanent magnetization. This partial ferromagnetic coupling, not surprisingly, results from the short circuits between the two Co layers.

Because the PLD trilayer has an atomically smooth interface with no such short circuits, the two Co layers are completely antiferromagnetically coupled which shows no remanent magnetization in both in-plane and perpendicular directions. As we addressed earlier, this should boost the GMR effect. Although similar Co/Cu/Co trilayer structure has also been obtained using surfactant assisted MBE growth [82], PLD is clearly advantageous in terms of both the simplicity and the generality of its applications. The Co/Cu/Co trilayer system presents a good example demonstrating how synthesis can make a real difference in magnetic properties of artificially structured materials.

Interestingly, instead of enhancing the sharpness of the interfaces, PLD has also been used to boost the columnar growth of permalloy (Py)/Ag multilayers for GMR application [107]. In this case, the GMR effect of the Py/Ag multilayers is promoted by the static antiferromagnetic ordering due to the presence of Py islands in the matrix of Ag [108,109]. This type of quasimultilayer configuration, when prepared by MBE [110] or sputter deposition [111], can only be achieved after a post-growth annealing. It was shown that the annealing process could be saved if the multilayers were grown by PLD with high fluence. The combined re-sputtering effect and the implantation effect of the high-energy ions in the plasma plume would create roughness most pronouncedly at the Py/Ag interface due to the high sputtering efficiency of Ag atoms. A GMR effect of up to 3.5% was observed in the as-grown Py/Ag multilayers.

4.2. High-density magnetic recording media

The ever-demanding miniaturization in magnetic recording media is pushing the areal density to be grown at a rate approaching 100% per annum. When the areal density goes beyond 100 Gbit/in.^{2}, two key factors of concern arise. These are the superparamagnetic effect (thermal stability) in the recording medium and the finite sensitivity of the readback head. Evidence has shown that magnetic thin films with large perpendicular magnetic anisotropy (PMA) are promising candidates for high-density magnetic recording media [112–115]. Of particular interest are a few fct $L1_0$ structured alloys including FePt, FePd, FeAu, and CoPt, which exhibit large PMA, a necessary requirement to achieve the magnetic stability in the high-density recording media.

The FePt or CoPt single-layer films with the ordered $L1_0$ fct structure appeared to be difficult to prepare by thin film deposition. For example, ordered FePt thin films were not obtained by either sputter deposition [116] or PLD [117]. However, by using PLD to grow $Fe_{50}Pt_{50}$/Ag multilayers on MgO(1 0 0) substrate, an ordered FePt with fct structure was formed after a post-growth annealing [117,118]. Fig. 33 shows the X-ray diffraction patterns of room temperature-grown ($Fe_{50}Pt_{50}$ (2 nm)/Ag
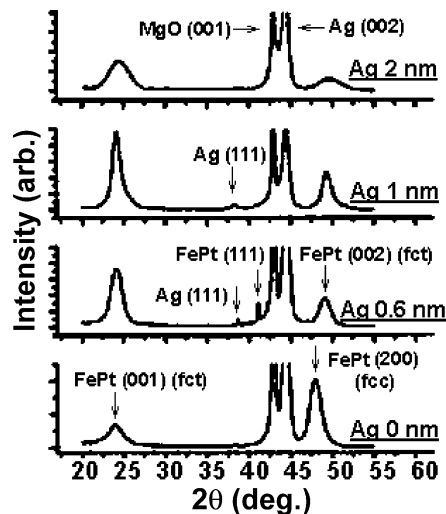

Fig. 33. X-ray diffraction patterns of 6 nm-thick FePt films with Ag layers inserted grown by PLD. The Ag layer thickness is shown in each panel. All samples were annealed at 630 °C for 15 min [117].
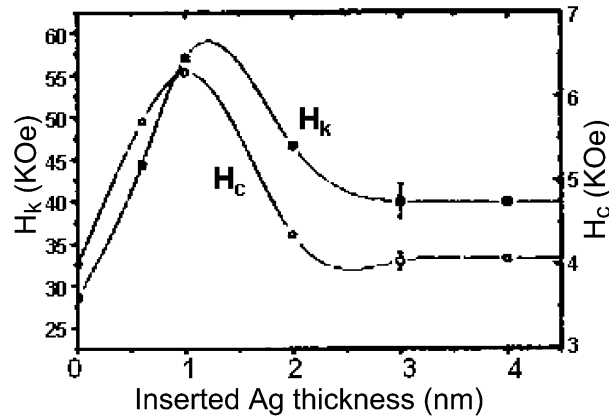
Fig. 34.   Magnetic coercivity (H_c) and magnetic anisotropy field (H_k) of the 6 nm-thick Ag-inserted FePt films (shown in Fig. 33) as a function of the inserted Ag layer thickness [117].

(x nm))$_3$ multilayers with various Ag layer thickness on MgO(1 0 0) substrates. All samples have been annealed at 630 °C for 15 min to enhance the $L1_0$ order. Apparently, without Ag spacer layers, FePt single layers are in a disordered fcc structure. When the Ag spacer layer thickness is higher than 0.6 nm, the fct $L1_0$ order appears. Consequently, as shown in Fig. 34, the magnetic anisotropy field and coercivity of the multilayers increases with increasing Ag thickness due to the improved chemical order in the FePt layers. The maximum effect seems to be reached at an Ag thickness of 1 nm. Similar experiments have also been performed on CoPt/C multilayers by PLD [119].

5. Congruent deposition of multicomponent magnetic alloys

Many magnetic materials with interesting properties are multicomponent alloys. To integrate magnetic materials in microelectronics, it is a necessity to grow the multicomponent alloys in thin films on, preferably, semiconductor substrates. Here, PLD holds its classical advantage of stoichiometric transfer of materials with complex composition. Even very complicated compounds such as Nd- and Cr-doped gadolinium–scandium–gallium garnet, which contains six elements and 160 atoms in a unit cell, can be grown epitaxially on Si(0 0 1) substrate [120]. In the following, we describe some recent applications of PLD in growing thin films of both soft and hard multicomponent magnetic alloys.

5.1. Fe- and Co-based amorphous alloys

Soft magnetic materials are used as flux guides in thin-film magnetic recording heads as well as magnetic field sensors. In this regard, Fe- and Co-based amorphous materials have superior magnetic properties with a combination of high permeability, high saturation magnetization, and low coercivity. In particular, the permeability of these materials can change orders of magnitude under a small magnetic field, causing strong variations in the internal fields and electrical current density, and consequently, on the impedance. This so-called giant magnetoimpedance (GMI) effect was first observed in amorphous Fe–Co–Si–B wires [121,122]. To integrate the GMI effect into microelectronic

devices, it is essential to grow thin films of amorphous Fe–Co–Si–B on Si substrates. Due to the complicated composition and structure of the amorphous magnetic materials, a congruent deposition technique has to be used. While both sputter deposition and PLD are suitable techniques, sputter deposition rarely produces thin films that fully retain the magnetic properties of commercial amorphous Fe–Co–Si–B ribbons or wires [123,124]. In contrast, PLD has shown enough versatility to allow the growth of high-quality thin films [125] of amorphous Fe–Co–Ni–Si–B on both Si and glass substrates. The films have comparable coercivity and anisotropy field values to those of the target amorphous ribbons, and much higher steepness of hysteresis loops. Fig. 35 shows hysteresis loops measured along hard (left) and easy (right) axis for a ribbon (upper) of $Fe_5Co_{60}Ni_{10}Si_{10}B_{15}$ and a 102 nm thick film on a Si substrate grown by PLD from the same ribbon. The much steeper hysteresis loops in the PLD films are induced by the large shape anisotropy in thin films, and also reflect the better structural homogeneity in the PLD films. The coercivity and the anisotropy field of the films could be easily tunable by controlling laser deposition parameters such as laser fluence [126], yet another advantage for PLD growth of soft magnetic thin films. Recently, the PLD grown amorphous magnetic thin films and multilayers have been used to construct prototype magnetic field sensors [127].

5.2. Rare earth–transition metal intermetallic compounds

Rare earth–transition metal compounds, such as $SmCo_5$ and $NdF_{14}B$, are the best commercially available permanent magnets in terms of the maximum energy product. Thin films of these hard magnetic alloys have potential applications in micromechanics [128], or form spring magnets when interfaced with thin films of soft magnetic materials [129]. To obtain large energy product in the grown hard magnetic thin films, it is important for the films to have both high uniaxial magnetic anisotropy and high coercivity simultaneously. The high uniaxial magnetic anisotropy requires proper stoichiometry and crystallographic texture of the films, while the high coercivity is associated with grain boundary properties in the films in addition to magnetic anisotropy. So far PLD has been applied to grow both Sm–Co [130,131] and Nd–Fe–B [132–136] thin films on various substrates, and achieved good success in terms of controlling the stoichiometry and crystallographic texture of the films. Engineering the grain boundaries in the thin films, however, appears to be more demanding. With the limited attempts, the coercivity of the PLD films has not been satisfactorily optimized. For example, PLD grown Sm–Co [137] and Nd–Fe–B films [131] exhibit coercivity of 2.2 and 1 T, respectively, which are lower than sputter deposited films. It is hopefully possible to further improve the coercivity of the PLD grown films by fine tuning laser settings such as fluence and repetition rate.

5.3. Half-Heusler alloy NiMnSb

Magnetic materials with high-spin polarization are most wanted for magnetoelectronic devices. Half-metallic materials are ideal candidates because they have 100% spin polarization at Fermi level. Half-Heusler alloy NiMnSb was predicted to belong to this class [138], and therefore has attracted interest to incorporate it into GMR or spin valve multilayer structures to enhance the magnetoresistance. The half metallicity of NiMnSb, however, is very sensitive to structural disorder. For this reason, a well-ordered crystallographic structure of the NiMnSb film is essential for device applications.

NiMnSb films have been grown by various deposition techniques that include rf magnetron sputtering [139], MBE [140], and PLD [141]. It appears that the films have to be grown at elevated
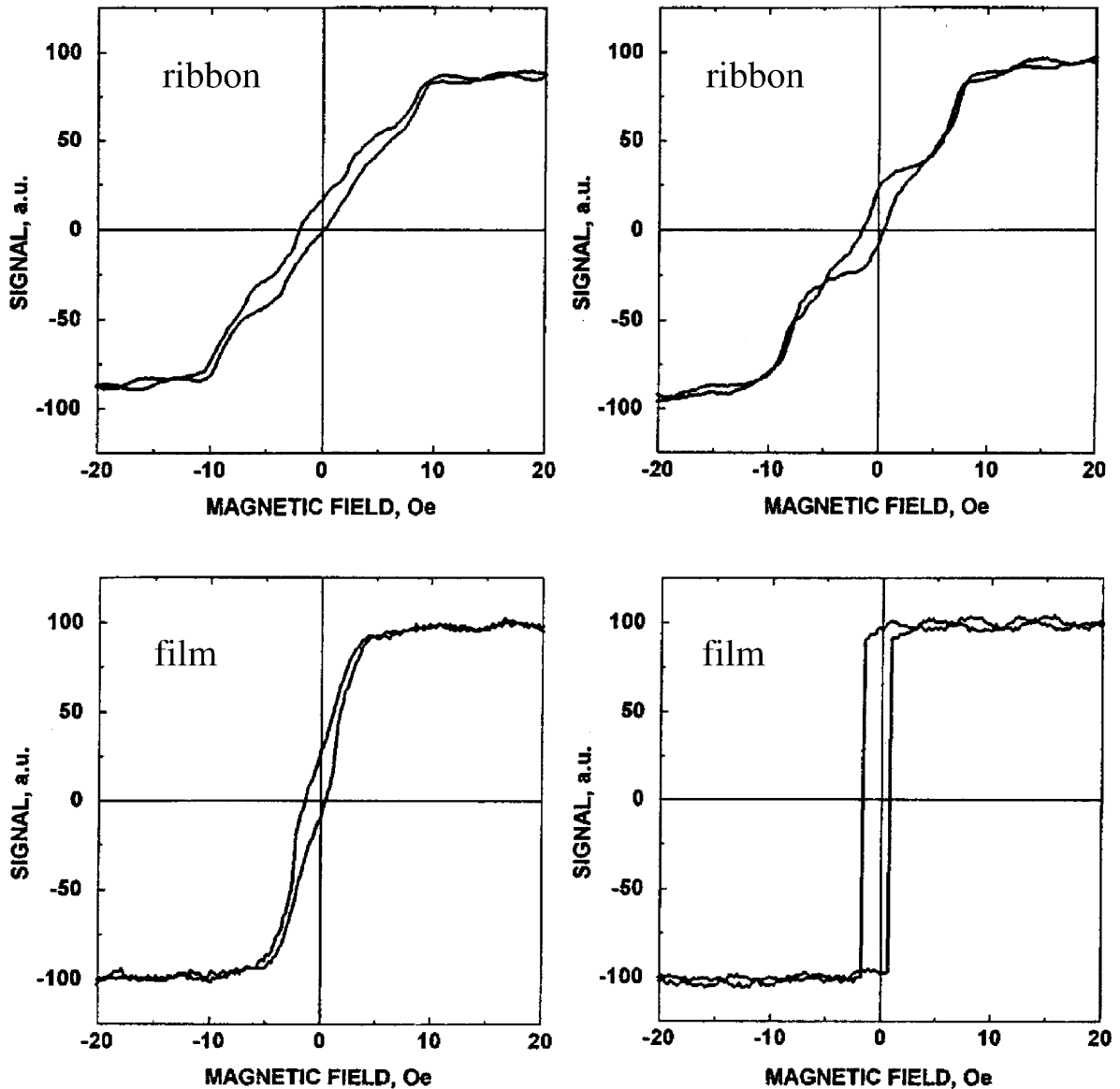
Fig. 35. Magnetic hysteresis loops measured along hard (left) and easy (right) axis for a ribbon (upper) of $Fe_5Co_{60}Ni_{10}Si_{10}B_{15}$ and a 102 nm-thick film on a Si substrate grown by PLD from the same ribbon [125].

temperatures in order to have a well-ordered $C1_b$ bulk crystal structure. However, high growth temperature is incompatible with spin valve or GMR devices due to the interdifffusion problem. Among all the attempts, PLD has been able to grow high-quality NiMnSb films at the lowest temperature (∼200 °C) so far [141]. Films grown on Si and InAs by PLD are all in single chemical phase, though the films on InAs substrate seem to have a better crystalline structure due to a smaller lattice mismatch.

6. New developments in PLD

6.1. Femtosecond pulsed-laser deposition

As mentioned in Section 2.1, when the laser pulse duration is reduced to sub-picosecond, i.e. shorter than the time scale of the electron–phonon coupling (a few picoseconds), the ablation process can be considered as direct solid–vapor (or solid–plasma) transition. Within a few picoseconds after the laser pulse, the vapor and plasma form and expand rapidly towards the vacuum side. Because the laser pulse terminates before the energy is completely redistributed in the target materials, ultrafast laser pulse tends to have a better ablation efficiency [142]. The ablation threshold for femtosecond pulses can be a factor of 10–100 lower than that of the nanosecond laser. This means that virtually all materials, including the most intractable materials such as refractory metals, can be cleanly and congruently ablated. The limited heating of the surrounding lattices of the target is also very useful for controlled material removal, which is turning the femtosecond laser into a powerful tool for surface microprocessing [143], micromachining [144], and surgical application [145].

The femtosecond laser is also beneficial for the growth of high-quality thin films in terms of elimination of droplets [146] and interesting enrichment of isotopes in the films [147]. The elimination of droplets was achieved by reduction of the single pulse energy to the point where fewer atoms are evaporated per pulse than those contained in a micron-sized cluster. The average deposition rate for the ultrafast PLD, however, can still be much faster than that for the nanosecond PLD by using a vastly higher repetition rate of $\sim$MHz. Smooth and droplet-free amorphous carbon films have been obtained in this way [148].

The most common femtosecond laser source is the amplified Ti:sapphire laser. Its repetition rate is typically limited in the range from tens of Hz to KHz. Recently, Reilly et al. have compared the thin film growth by femtosecond free electron laser and by the amplified Ti:sapphire laser [149]. The Thomas Jefferson National Accelerator Facility Free Electron Laser (TJNAF-FEL) used in this study allows a high tunability of laser pulses. The TJNAF-FEL can be operated in both pulsed modes at repetition rates up to 1 kHz, and cw mode with a continuous train of micropulses at 18.7, 37.4, or 74.8 MHz. Thin magnetic films of $Ni_{80}Fe_{20}$ were grown on Si substrates by both TJNAF-FEL (37.4 MHz, pulse energy 5 μJ) and a Ti:sapphire laser (1 kHz, pulse energy 0.7 mJ) for comparison. Significant improvement of morphology, structure and magnetic behavior were observed in the films grown by TJNAF-FEL. Fig. 36 shows the SEM (upper) and AFM (lower) images of the films grown by Ti:sapphire (left) and FEL (right) lasers. The Ti:sapphire PLD film has a roughness of $\sim$275 Å, which is more than six times higher than that of the FEL PLD film ($\sim$44 Å). The XRD peaks shown in Fig. 37 also confirm a better crystallinality for the FEL PLD film, which displays stronger and sharper diffraction peaks.

With the improved morphology and crystallographic structure, the FEL PLD film shows well-defined rectangular hysteresis loops with small coercivity, as shown in Fig. 38. In contrast, the Ti:sapphire PLD film has a much higher coercivity and lower M_r/M_s ratio due to its granular morphology. Remarkably, these improvements were achieved with the FEL deposition rate (17 Å/s) being considerably higher than that of the Ti:sapphire laser (1 Å/s). This shows that increasing the repetition rate while reducing the energy per pulse in PLD is very beneficial for better thin film quality. Undoubtedly, femtosecond laser PLD, particularly using the FEL, offers new flexibility to control the quality of films, especially for the growth of magnetic multilayers.
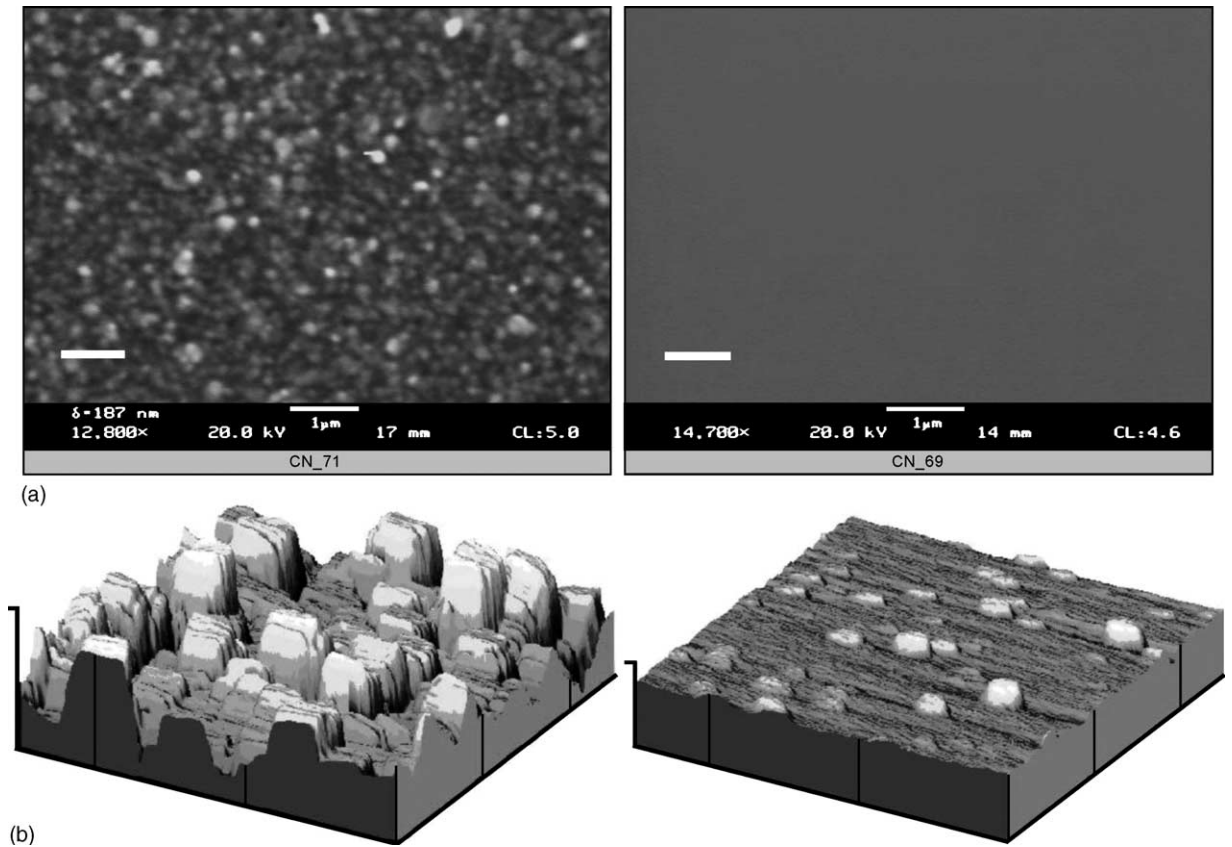
Fig. 36. SEM (top) and AFM (bottom) scans for $Ni_{80}Fe_{20}$ thin films grown with (a) the amplified Ti:sapphire system (left pictures) and (b) the TJNAF-FEL (right pictures). For the SEM scans, magnification ~13,000 (the white line indicates 1 μm). For the AFM scans, dimensions are 5 μm square and the line indicates 1500 Å height (courtesy from A. Reilly).
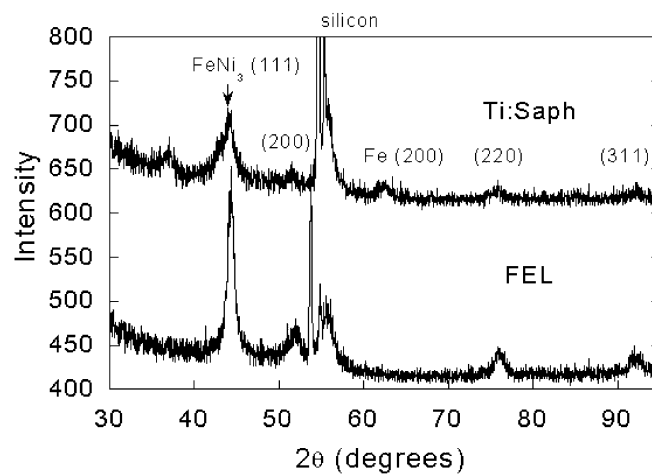

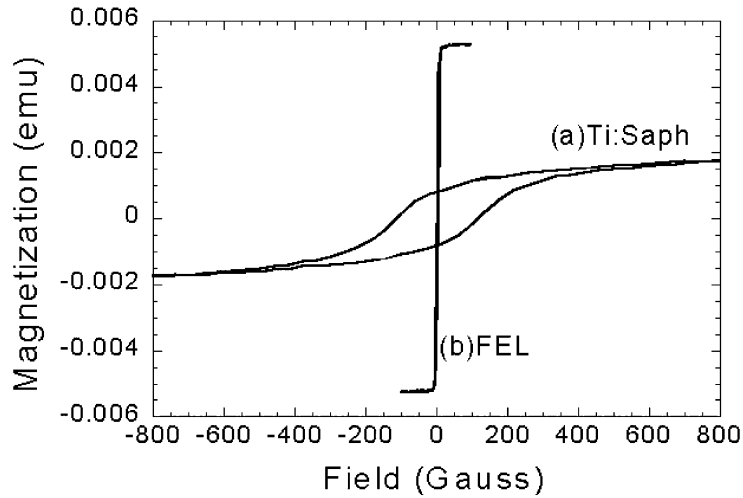Fig. 37. XRD spectra for $Ni_{80}Fe_{20}$ thin films grown with amplified Ti:sapphire (top) and FEL (bottom) (courtesy from A. Reilly).

Fig. 38. Magnetization curves for $Ni_{80}Fe_{20}$ thin films produced with the (a) amplified Ti:sapphire system and (b) the FEL (courtesy from A. Reilly).

6.2. Metallic nanostructures

Most of our previous sections have been devoted to describe the power of PLD to grow smooth films and multilayers. In this section, however, we will show that PLD is also a valuable tool to grow metallic nanostructures when conditions are set right. There are generally three types of approaches to grow metallic nanostructures, including: (1) shadow deposition onto patterned substrates formed by self-assembly or self-organization, (2) direct deposition on substrates that allow the Vollmer–Weber growth, and (3) formation of nano-particles in a laser plume in an ambient pressure of inert gases or in solutions. In addition, pulsed laser beams can also be used to create nanostructures by direct laser interference lithography [150,151].

Using PLD shadow deposition to create nanostructures requires a substrate that has pre-made patterns at nanometer scale. Such patterns are often formed by self-organization or self-assembly. For example, a family of self-organized structures has been found in $Si_{1-x}Ge_x$ thin films grown on Si(0 0 1) substrate [152,153]. Fig. 39(a) shows an AFM image of a 2.5 nm $Si_{0.55}Ge_{0.45}$ thin film grown on a vicinal Si(0 0 1) surface (4° towards [1 1 0] direction). The triangular-shaped nanostructures consist three types of nanofacets, i.e. ($\bar{1}$ 0 5), (0 $\bar{1}$ 5), and (0 0 1), as schematically shown in Fig. 39(b). Such a surface is a perfect template to fabricate two-dimensional arrays of nanomagnets because magnetic films can be grown on only one selected facet under grazing incidence.

To achieve the 2D nanomagnetic array with the highest quality, it is important to grow smooth magnetic films on the selected facet. This naturally makes PLD the best choice for growth. Teichert et al. have used PLD to grow 2 nm Cu/2 nm Co/2 nm Cu trilayers on the ($\bar{1}$ 0 5) facets at the deposition angle of 5° towards [1 0 0] direction. The SEM morphology of the 2D array of Co/Cu trilayer is compared with a continuous Co/Cu trilayer film formed by normal incidence in Fig. 40(a) and (b), respectively. While the continuous film in Fig. 40(b) does not show any distinct contrast in SEM, the higher secondary electron yield lets the Co covered ($\bar{1}$ 0 5) facets, i.e. the Co nanomagnets, appear as bright patches in Fig. 40(a).
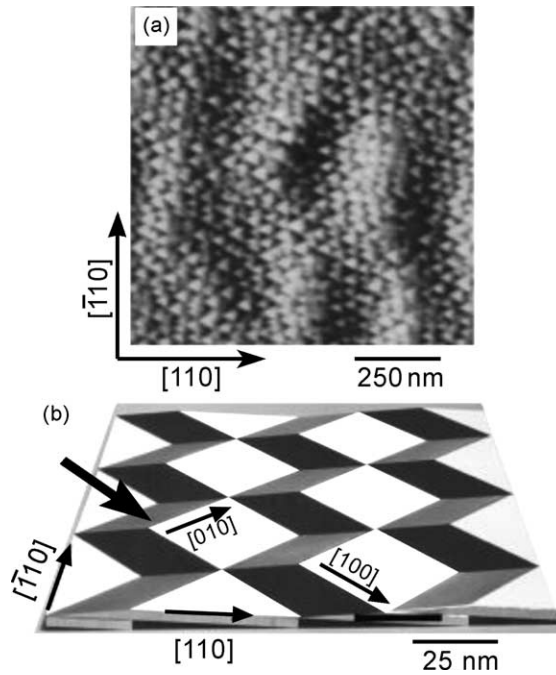
Fig. 39.   2.5 nm Si$_{0.55}$Ge$_{0.45}$ film grown on a vicinal Si(0 0 1) substrate with a 4° miscut towards the [1 1 0] direction: (a) gray-scale AFM image; (b) three-dimensional model of the surface morphology. The white areas represent (1 0 0) terraces, the gray and black areas correspond to ($\bar{1}$ 0 5) and (0 $\bar{1}$ 5) facets, respectively. The indicated deposition geometry (black arrow) results in an array of parallelogram-like Co patches on the ($\bar{1}$ 0 5) facets [154].
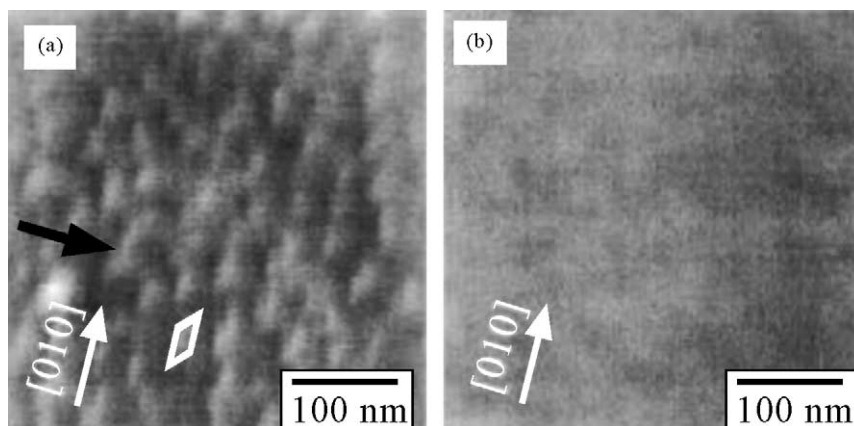

Fig. 40.   360 nm × 360 nm SEM images of the template shown in Fig. 39(a) after shadow deposition (a) and normal incidence deposition (b) of a 2 nm Co/2 nm Cu sandwich. The black arrow in (a) denotes the (projected) orientation of the evaporation [154].
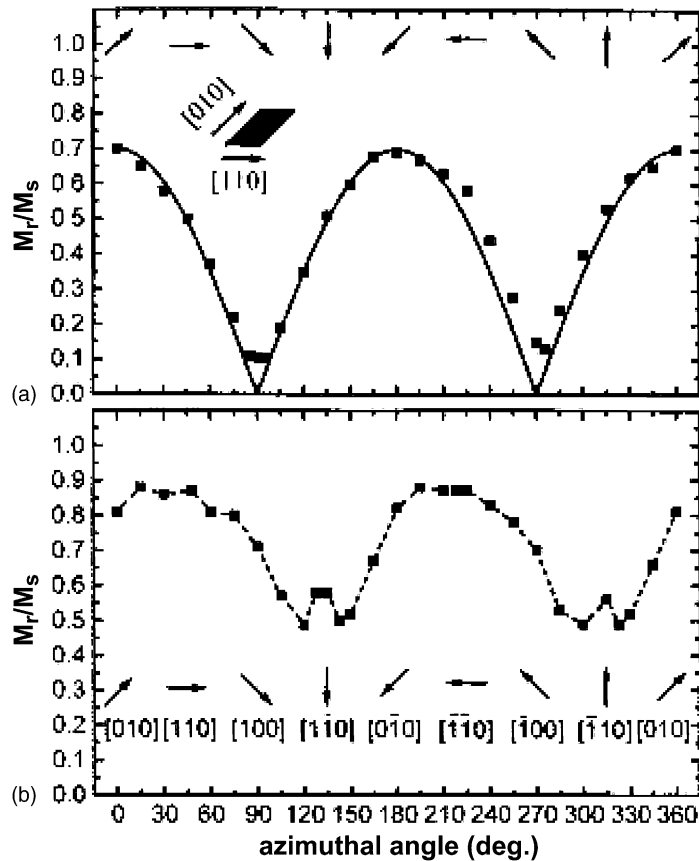
Fig. 41. Squareness (M_r/M_s) of the in-plane hysteresis loops as a function of sample orientation for the shadow deposited sample (a) and the continuous Co film (b). Arrows and the inset are shown to identify the orientation of the magnetic field with respect to the nanostructures for a given azimuthal angle ϕ. The solid line in (a) represents $|\cos(\phi)|$ scaled to the maximum of M_r/M_s [154].

The magnetic measurements of the 2D array of the Co/Cu trilayer indicate a significantly enhanced uniaxial anisotropy as compared with that of the continuous Co/Cu trilayer. Fig. 41 shows the remanence versus saturation (M_r/M_s) ratio of a 2D array (a) and a continuous film (b) recorded by longitudinal MOKE (field applied parallel to the macroscopic plane). The nanomagnets show strong uniaxial anisotropy with their easy axis along [0 1 0] or [0 $\bar{1}$ 0] direction, and exhibits no remanence along the hard axis directions ([1 0 0] and [$\bar{1}$ 0 0]). This is stark contrast to the rather isotropic magnetic behavior of the continuous film. The origin of the uniaxial anisotropy [154] along the [0 1 0] direction was proposed to be a result of the uniformly aligned steps of the ($\bar{1}$ 0 5) facet, which are along [0 1 0] direction.

Another interesting attempt to grow magnetic nanostructures is to use substrates that have considerably lower surface free energy than that of the 3d magnetic elements (Fe, Co, Ni). These include most of the oxides and nitrides. The so-called Vollmer–Weber or three-dimensional growth is promoted at relatively high growth temperatures to minimize the cost of total surface free energy. For Si
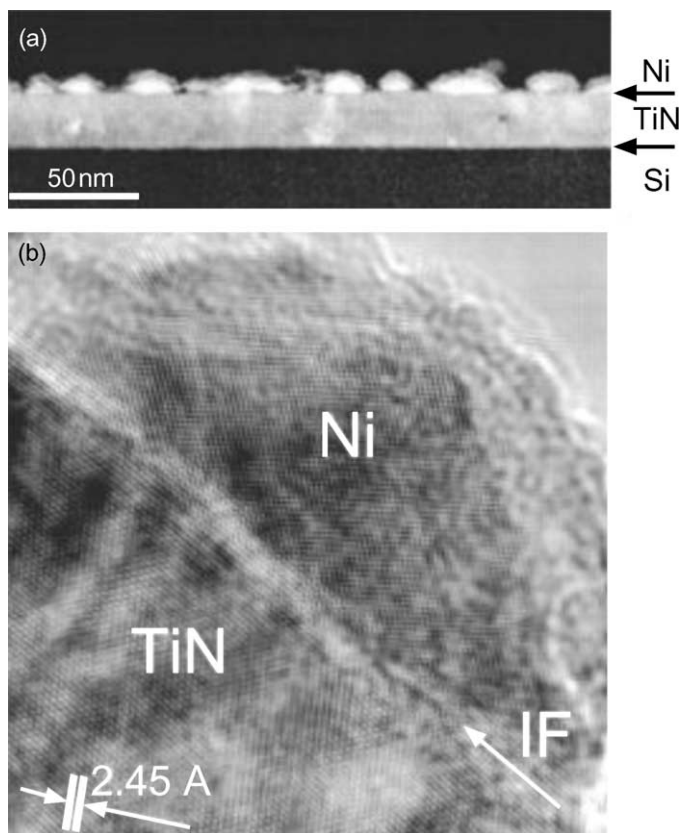
Fig. 42.   (a) A cross-sectional STEM-Z image of Ni nanocrystallites in TiN matrix and (b) high-resolution STEM-Z contrast image of the same sample (courtesy from J. Narayan).

compatibility, the oxides or nitrides layers should be grown, preferably epitaxially, on Si substrate prior to the growth of magnetic nanostructures. Under such conditions, PLD is a convenient method to use to grow both oxides (nitrides) and magnetic elements in one vacuum system.

Using this approach, Kumar et al. have grown nanocrystalline Ni crystallites embedded in a TiN matrix by alternatively depositing Ni and TiN on Si at 600 °C [155]. Fig. 42 shows the cross-sectional STEM-Z image of Ni particles in a TiN matrix in (a), and the high-resolution STEM image of a Ni nanocrystallite in $\langle 1\,1\,0 \rangle$ cross-section in (b). The Ni particles are well separated with an average dimension of 17 nm in base and 9 nm in height. The Ni nanocrystallites were observed to be textured with two distinct epitaxial relationships with TiN, which are either cube-on-cube in TiN or have a 90° rotation with respect to TiN[1 1 0] direction. These textured Ni nanocrystallites were compared with random-oriented Ni nanodots (grown in amorphous Al_2O_3 matrix) in terms of magnetic behavior. As shown in Fig. 43, the textured Ni nanocrystallites have a much higher blocking temperature (~275 K) than that of the random-oriented Ni nanodots (~100 K). The increase of the blocking temperature reflects the enhanced magnetic anisotropy in the textured nanodot system.

Both of the previous two approaches rely on the proper choice of substrates. A more generic approach is to form clusters or nanodots in the laser plume before landing on the substrate. This can be
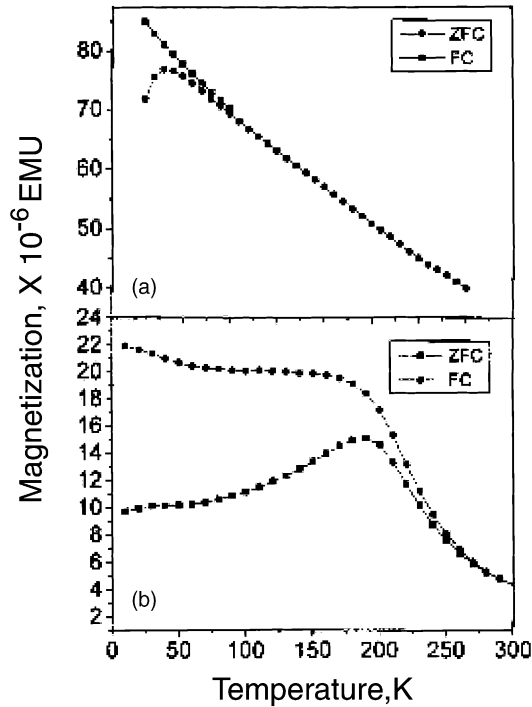
Fig. 43. ZFC and FC magnetization data as a function of temperature for Ni nanocrystallites in (a) amorphous Al_2O_3 and (b) crystal TiN samples (courtesy from J. Narayan).

shown by PLD in ambient gases [156–158] or even in solutions [159,160]. It was observed that the formed clusters concentrated in a limited region in the plume, possibly due to the convection within the plume [161]. This type of spatial distribution of the clusters implies that the cluster growth will be significantly affected by PLD conditions including the substrate–target distance. Also, at least in solution it was demonstrated that femtosecond laser pulses produce more uniform-sized dots than nanosecond laser pulses do [162].

7. Concluding remarks and outlook

With all the examples presented in this paper, we can conclude that PLD is a highly useful technique to grow metallic thin films and multilayers. In particular, PLD has shown great strength in the following four areas of growth: (1) growing high-quality thin films in a layer-by-layer mode; (2) stabilizing highly metastable or even unstable structures in thin films; (3) congruently depositing multi-component films; (4) providing high flexibility of tuning deposition parameters during growth. These advantages, coupled with the simplicity and versatility of its operation, should make PLD a more and more popular method for the growth of metallic thin films and multilayers. With the increasing availability of femtosecond laser sources, ultrafast PLD will perhaps become the growth technique for metals.

Beyond films, PLD has also shown good potential for fabricating smaller nanostructures. Even though current efforts have met with limited success, it is clear that PLD is a suitable technique for this

type of research. The high tunability of PLD will be the decisive factor that allows the future success of PLD in nanostructure synthesis.

Acknowledgements

References

[1] J.A.C. Bland, B. Heinrich, Ultrathin Magnetic Structures, Springer-Verlag, Berlin, 1994.

[2] J. Shen, J. Kirschner, Surf. Sci. 500 (2002) 300.

[3] S. Bader, Surf. Sci. 500 (2002) 172.

[4] M.N. Baibich, J.M. Broto, A. Fert, F. Nguyen Van Dau, F. Petroff, P. Etienne, G. Creuzet, A. Friederich, J. Chazelas, Phys. Rev. Lett. 61 (1988) 2472.

[5] G. Binasch, P. Grunberg, F. Saurenbach, W. Zinn, Phys. Rev. B 39 (1989) 4828.

[6] T. Miyazaki, N. Tezuka, J. Magn. Magn. Mater. 139 (1995) L231.

[7] J.S. Moodera, L.R. Kinder, T.M. Wong, R. Meservey, Phys. Rev. Lett. 74 (1995) 3273.

[8] F. Matsukura, H. Ohno, A. Shen, Y. Sugawara, Phys. Rev. B 57 (1998) R2037.

[9] A. Haury, A. Wasiela, A. Arnoult, J. Cibert, S. Tatarenko, T. Dietl, Y. Merle d'Aubigne, Phys. Rev. Lett. 79 (1997) 511.

[10] Y.D. Park, A.T. Hanbicki, S.C. Erwin, C.S. Hellberg, J.M. Sullivan, J.E. Mattson, T.F. Ambrose, A. Wilson, G. Spanos, B.T. Jonker, Science 295 (2002) 651.

[11] T. Dietl, Semicond. Sci. Technol. 17 (2002) 377.

[12] B. Lee, T. Jungwirth, A.H. MacDonald, Semicond. Sci. Technol. 17 (2002) 393.

[13] S.A. Wolf, D.D. Awschalom, R.A. Buhrman, J.M. Daughton, S. von Molnar, M.L. Roukes, A.Y. Chtchelkanova, D.M. Treger, Science 294 (2001) 1488.

[14] X.W. Li, A. Gupta, X. Gang, Appl. Phys. Lett. 75 (1999) 711.

[15] D.B. Chrisey, G.K. Hubler (Eds.), Pulsed Laser Deposition of Thin Films, Wiley, New York, 1994;
P.R. Willmott, J.R. Huber, Rev. Mod. Phys. 72 (2000) 315.

[16] D. Dijkkamp, T. Venkatesan, X.D. Wu, S.A. Shaheen, N. Jisrawi, Y.H. Min-Lee, W.L. Mclean, M. Croft, Appl. Phys. Lett. 51 (1987) 619.

[17] H. Schwartz, H.A. Tourtellotte, J. Vac. Sci. Technol. 6 (1969) 373.

[18] Yu.A. Bykovskii, V.M. Boyakov, V.T. Galochkin, A.S. Molchanov, I.N. Nikolaev, A.N. Oraevskii, Sov. Phys. Tech. Phys. 23 (1978) 578.

[19] H. Jenniches, M. Klaua, H. Höche, J. Kirschner, Appl. Phys. Lett. 69 (1996) 3339.

[20] O.F.K. McGrath, F. Robaut, N. Cherief, A. Lienard, M. Brunel, D. Givord, Surf. Sci. 315 (1994) L1017.

[21] O. Fruchart, S. Jaren, J. Rothman, Appl. Surf. Sci. 135 (1998) 218.

[22] S. Kahl, H.-U. Krebs, Phys. Rev. B 63 (2001) 172103.

[23] J. Shen, P. Ohresser, Ch.V. Mohan, M. Klaua, J. Barthel, J. Kirschner, Phys. Rev. Lett. 80 (1998) 1980.

[24] J.C.S. Kools, in: D.B. Chrisey, G.K. Hubler (Eds.), Pulsed Laser Deposition of Thin Films, Wiley, New York, 1994, pp. 455–471.

[25] H.U. Krebs, Int. J. Non-Equilib. Pr. 10 (1997) 3.

[26] P.P. Pronko, S.K. Dutta, D. Du, J. Appl. Phys. 78 (1995) 6233.

[27] R. Timm, P.R. Willmott, J.R. Huber, J. Appl. Phys. 80 (1996) 1794.

[28] R.W. Dreyfus, J. Appl. Phys. 69 (1991) 1721.

[29] J.C.S. Kools, S.H. Brongersma, E. van de Riet, J. Dieleman, Appl. Phys. B 53 (1991) 125.

[30] P.E. Dyer, Appl. Phys. Lett. 55 (1989) 1630.

[31] J. Lunney, Appl. Surf. Sci. 88 (1995) 79.

[32] N. Cherief, D. Givord, O.F.K. McGrath, Y. Otani, F. Robaut, J. Magn. Magn. Mater. 126 (1993) 225.

[33] J.A. Venables, Philos. Mag. 17 (1973) 697.

[34] H. Brune, Surf. Sci. Rep. 31 (1998) 121.

[35] P.-O. Jubert, O. Fruchart, C. Meyer, Surf. Sci. 522 (2003) 8.

[36] J.E. Prieto, J. de la Figuera, R. Miranda, Phys. Rev. B 62 (2000) 2126.

[37] N. Combe, P. Jensen, Phys. Rev. B 57 (1998) 15553.

[38] P. Jensen, B. Niemeyer, Surf. Sci. Lett. 384 (1997) L823.

[39] B. Hinnemann, H. Hinrichsen, D.E. Wolf, Phys. Rev. Lett. 87 (2001) 135701.

[40] P.-M. Lam, S.J. Liu, C.H. Woo, Phys. Rev. B 66 (2002) 45408.

[41] S.B. Lee, Phys. Rev. E 67 (2003) 012601.

[42] L.H. Tang, J. Phys. I 3 (1993) 935.

[43] J.G. Amar, F. Family, P.-M. Lam, Phys. Rev. B 50 (1994) 8781.

[44] B. Hinnemann, H. Hinrichsen, D.E. Wolf, Phys. Rev. B 67 (2003) 11602.

[45] H. Jenniches, M. Klaua, H. Höche, J. Kirschner, Appl. Phys. Lett. 69 (1996) 3339.

[46] O. Fruchart, S. Jaren, J. Rothman, Appl. Surf. Sci. 135 (1998) 218.

[47] Y.G. Li, A.E. DePristo, Surf. Sci. 319 (1994) 141.

[48] X.W. Zhou, H.N.G. Wadley, Surf. Sci. 431 (1999) 42.

[49] C.M. Gilmore, J.A. Sprague, Phys. Rev. B 44 (1991) 8950.

[50] Y. Yue, Y.K. Ho, Z.Y. Pan, R.W. Lee, Z.Y. Man, J. Xie, Phys. Lett. A 235 (1997) 267.

[51] N. Levanov, V.S. Stepanyuk, W. Hergert, O.S. Trushin, K. Kokko, Surf. Sci. 400 (1998) 54.

[52] G. Rosenfeld, R. Servaty, C. Teichert, B. Poelsema, G. Comsa, Phys. Rev. Lett. 71 (1993) 895.

[53] J. Kirschner, H. Engelhard, D. Hartung, Rev. Sci. Instrum. 73 (2002) 3853.

[54] R.P. van Ingen, R.H.J. Fastenau, E.J. Mittemeijer, Phys. Rev. Lett. 72 (1994) 3116.

[55] H.U. Krebs, M. Störmer, Phys. Rev. Lett. 75 (1995) 3966.

[56] R.P. van Ingen, R.H.J. Fastenau, E.J. Mittemeijer, Phys. Rev. Lett. 75 (1995) 3967.

[57] T.B. Massalski, H. Okamoto, P.R. Sabramamian, L. Kacprzak (Eds.), Binary Alloy Phase Diagrams, 2nd ed., vol. 1, ASM International, Materials Park, OH, 1990, p. 64.

[58] C.S. Wang, B.M. Klein, H. Krakauer, Theory of magnetic and structural ordering in iron, Phys. Rev. Lett. 54 (1985) 1852.

[59] F.J. Pinski, J. Staunton, B.L. Gyorffy, D.D. Johnson, G.M. Stocks, Ferromagnetism versus aniferromagnetism in face-centered-cubic iron, Phys. Rev. Lett. 56 (1986) 2096.

[60] V.L. Moruzzi, P.M. Marcus, K. Schwarz, P. Mohn, Ferromagnetic phases of bcc and fcc Fe, Co, and Ni, Phys. Rev. B 34 (1986) 1784.

[61] S.C. Abrahams, L. Cuttman, J.S. Kasper, Phys. Rev. 127 (1962) 2052;
G.J. Johanson, M.B. McGirr, D.A. Wheeler, Phys. Rev. B 1 (1970) 3208.

[62] U. Gradmann, P. Tillmanns, Phys. Status Solidi (a) 44 (1977) 539.

[63] A. Kirilyuk, J. Giergiel, J. Shen, M. Straub, J. Kirschner, Phys. Rev. B 54 (1996) 1050.

[64] C.C. Kuo, W. Pan, Y.C. Chen, M.T. Lin, J. Appl. Phys. 93 (2003) 8743.

[65] J. Thomassen, F. May, B. Feldmann, M. Wuttig, H. Ibach, Phys. Rev. Lett. 69 (1992) 3831.

[66] D. Li, M. Freitag, J. Pearson, Z.Q. Qiu, S.D. Bader, Phys. Rev. Lett. 72 (1994) 3112.

[67] D.J. Keavney, D.F. Storm, J.W. Freeland, I.L. Grigorov, J.C. Walker, Phys. Rev. Lett. 74 (1995) 4531.

[68] R.D. Ellerbrock, A. Fuest, A. Schatz, W. Keune, R.A. Brand, Phys. Rev. Lett. 74 (1995) 3053.

[69] D. Qian, X.F. Jin, J. Barthel, M. Klaua, J. Kirschner, Phys. Rev. Lett. 87 (2001) 227204.

[70] S. Müller, P. Bayer, C. Reischl, K. Heinz, B. Feldmann, H. Zillgen, M. Wuttig, Phys. Rev. Lett. 74 (1995) 765.

[71] A. Biedermann, R. Tscheließnig, M. Schmid, P. Varga, Phys. Rev. Lett. 87 (2001) 86103.
[72] J. Shen, H. Jenniches, Ch.V. Mohan, J. Barthel, M. Klaua, P. Ohresser, J. Kirschner, Europhys. Lett. 43 (1998) 349.
[73] H. Jenniches, J. Shen, Ch.V. Mohan, S. Sundar Manoharan, J. Barthel, P. Ohresser, M. Klaua, J. Kirschner, Phys. Rev. B 59 (1999) 1196.
[74] M. Weinelt, S. Schwarz, H. Baier, S. Müller, L. Hammer, K. Heinz, Th. Fauster, Phys. Rev. B 63 (2001) 205413.
[75] A. Kirilyuk, J. Giergiel, J. Shen, M. Straub, J. Kirschner, Phys. Rev. B 54 (1996) 1050.
[76] J. Shen, J.P. Pierce, E.W. Plummer, J. Kirschner, J. Phys.: Condens. Matter 15 (2003) R1.
[77] J. Shen, M. Klaua, P. Ohresser, H. Jenniches, J. Barthel, Ch.V. Mohan, J. Kirschner, Phys. Rev. B 56 (1997) 11134.
[78] P. Ohresser, J. Shen, J. Barthel, M. Zheng, Ch.V. Mohan, M. Klaua, J. Kirschner, Phys. Rev. B 59 (1999) 3696.
[79] B Ujfalussy, Private communication.
[80] M. Hansen (Ed.), Constitution of Binary Alloys, McGraw-Hill, New York, 1958, p. 471ff.
[81] J. Fassbender, U. May, B. Schirmer, R.M. Jungblut, B. Hillebrands, G. Guntherodt, Phys. Rev. Lett. 75 (1995) 4476.
[82] J. Camarero, T. Graf, J.J. de Miguel, R. Miranda, W. Kuch, M. Zharnikov, A. Dittschar, C.M. Schneider, J. Kirschner, Phys. Rev. Lett. 76 (1996) 4428.
[83] K. Takanashi, S. Mitani, M. Sano, H. Fujimori, H. Nakajima, A. Osawa, Appl. Phys. Lett. 67 (1995) 1016.
[84] K. Takanashi, K. Himi, S. Mitani, M. Yamaguchi, D.H. Ping, K. Hono, H. Fujimori, Surf. Sci. 493 (2001) 713.
[85] M. Dynna, A. Marty, B. Gilles, G. Patrat, Acta Mater. 45 (1997) 257.
[86] G. Abadias, I. Schuster, A. Marty, B. Gilles, T. Deutsch, J. Cryst. Growth 222 (2001) 685.
[87] T. Shima, T. Moriguchi, S. Mitani, K. Takanashi, Appl. Phys. Lett. 80 (2002) 288.
[88] K. Sumiyama, T. Yoshitabe, Y. Nakamura, J. Phys. Soc. Jpn. 53 (1984) 2160.
[89] C.L. Chien, S.H. Liou, D. Kofalt, W. Yu, T. Eqami, T.R. McGuire, Phys. Rev. B 33 (1986) 3247.
[90] P. Crespo, A. Hernando, A.R. Yavari, O. Drbohlar, A.G. Escorial, J.M. Baranidaran, I. Oruc, Phys. Rev. B 48 (1993) 7134.
[91] T. Ambrose, A. Gavrin, C.L. Chien, J. Magn. Magn. Mater. 124 (1993) 15.
[92] V.G. Harris, K.M. Kemmer, B.N. Das, N.C. Koon, A.E. Ehrlich, J.P. Kirkland, J.C. Woicik, P. Crespo, A. Hernando, A.G. Escorial, Phys. Rev. B 54 (1996) 6929.
[93] J. Giergiel, J. Kirschner, J. Landgraf, J. Shen, J. Woltersdorf, Surf. Sci. 310 (1994) 1.
[94] W. Pitch, Philos. Mag. 4 (1959) 577.
[95] S.S. Manoharan, M. Klaua, J. Shen, J. Barthel, H. Jenniches, J. Kirschner, Phys. Rev. B 58 (1998) 8549.
[96] W. Kuch, M. Salvietti, X. Gao, M.-T. Lin, M. Klaua, J. Barthel, Ch.V. Mohan, J. Kirschner, Phys. Rev. B 58 (1998) 8556.
[97] J.M. MacLaren, T.C. Schulthess, W.H. Butler, R. Sutton, M. McHenry, J. Appl. Phys. 85 (1999) 4833.
[98] G.A. Farnan, C.L. Fu, Z. Gai, M. Krcmar, A.P. Baddorf, Z.Y. Zhang, J. Shen, Phys. Rev. Lett. 91 (2003) 226106.
[99] J.C.S. Kools, R. Coehoorn, F.J.G. Hakkens, R.H.J. Fastenau, J. Magn. Magn. Mater. 121 (1993) 83.
[100] M. Enrech, J.G. Lunney, R. Skomski, J.M.D. Coey, Mater. Sci. Eng. B 23 (1994) 25.
[101] N. Cherief, D. Givord, A. Liénard, K. Mackay, O.F.K. McGrath, J.P. Rebouillat, F. Robaut, Y. Souche, J. Magn. Magn. Mater. 121 (1993) 94.
[102] O. Fruchart, J.P. Nozieres, D. Givord, J. Magn. Magn. Mater. 207 (1999) 158.
[103] M.N. Baibich, J.M. Broto, A. Fert, F. Nguyen Van Dau, F. Petroff, P. Etienne, G. Creuzet, A. Friederich, J. Chazelas, Phys. Rev. Lett. 61 (1988) 2472.
[104] G. Binasch, P. Grunberg, F. Saurenbach, W. Zinn, Phys. Rev. B 39 (1989) 4828.
[105] W.H. Butler, X.-G. Zhang, D.M.C. Nicholson, Phys. Rev. Lett. 76 (1996) 3216.
[106] R. Gupta, M. Weisheit, H.-U. Krebs, P. Schaaf, Phys. Rev. B 67 (2003) 75402.
[107] J. Faupel, H.U. Krebs, A. Käufler, Y. Luo, K. Samwer, S. Vitta, J. Appl. Phys. 92 (2002) 1171.
[108] M.A. Parker, T.L. Hylton, K.R. Coffey, J.K. Howard, J. Appl. Phys. 75 (1994) 6382.
[109] J.A. Borchers, P.M. Gehring, R.W. Erwin, C.F. Majkrzak, J.F. Ankner, T.L. Hylton, K.R. Coffey, M.A. Parker, J.K. Howard, J. Appl. Phys. 79 (1996) 4762.
[110] R.F.C. Farrow, R.F. Marks, T.A. Rabedeau, M.F. Toney, D. Dobbertin, R. Beyers, S.S.P. Parkin, J. Appl. Phys. 76 (1994) 3688.
[111] T.L. Hylton, K.R. Coffey, M.A. Parker, J.K. Howard, J. Appl. Phys. 75 (1994) 7058.
[112] R. Wood, IEEE Trans. Magn. 36 (2000) 36.

[113] Y. Nakamura, S. Yamamoto, S. Iwasaki, IEEE Trans. Magn. 22 (1986) 376.

[114] H. Muraoka, Y. Nakamura, J. Magn. Soc. Jpn. 21-S2 (1997) 157.

[115] S. Iwasaki, Y. Nakamura, K. Ouchi, IEEE Trans. Magn. 15 (1979) 1456.

[116] T. Suzuki, T. Kiya, N. Honda, K. Ouchi, IEEE Trans. Magn. 36 (2000) 2417.

[117] Z. Zhang, K. Kang, T. Suzuki, J. Appl. Phys. 93 (2003) 7163.

[118] T. Yang, E. Ahmad, T. Suzuki, J. Appl. Phys. 91 (2002) 6860.

[119] S. Stavroyiannis, I. Panagiotopoulos, D. Niarchos, J.A. Christodoulides, Y. Zhang, G.C. Hadjipanayis, J. Magn. Magn. Mater. 193 (1999) 181;
S. Stavroyiannis, I. Panagiotopoulos, D. Niarchos, J.A. Christodoulides, Y. Zhang, G.C. Hadjipanayis, J. Appl. Phys. 91 (2002) 6860.

[120] P.R. Willmott, P. Manoravi, K. Holliday, Appl. Phys. A: Mater. 70 (2000) 425.

[121] R.S. Beach, A.E. Berkowitz, Appl. Phys. Lett. 64 (1994) 3652.

[122] L.V. Panina, K. Mohri, Appl. Phys. Lett. 65 (1994) 1189.

[123] R. Banerjee, G. Choe, B.-II. Cho, R. Walser, IEEE Trans. Magn. 31 (1995) 3856.

[124] G. Rieger, G. Rupp, G. Gieres, R. Losehand, W. Hartung, R. Losehand, W. Hartung, J. Appl. Phys. 91 (2002) 8447.

[125] P.I. Nikitin, A.A. Beloglazov, A.Yu. Toporov, M.V. Valeiko, V.I. Konov, A. Perrone, A. Luches, L. Mirenghi, L. Tapfer, J. Appl. Phys. 82 (1997) 1408.

[126] M. Sorescu, L. Tsakalakos, T. Sands, J. Appl. Phys. 85 (1999) 6652.

[127] P.I. Nikitin, S.I. Kasatkin, A.M. Muravjov, P.M. Vetoshko, M.V. Valeiko, V.I. Konov, T. Meydan, Sens. Actuators A: Phys. 106 (2003) 26.

[128] S. Yamashita, J. Yamasaki, M. Ikeda, N. Iwabuchi, J. Appl. Phys. 70 (1991) 6627.

[129] J.S. Jiang, E.E. Fullerton, C.H. Sowers, A. Inomata, S.D. Bader, A.J. Shapiro, R.D. Shull, V.S. Gornakov, V.I. Nikitenko, IEEE Trans. Magn. 35 (1999) 3229.

[130] F.J. Cadieu, R. Rani, X.R. Qian, L. Chen, J. Appl. Phys. 83 (1998) 6247.

[131] V. Neu, U. Hannermann, S. Fahler, B. Holzapfel, L. Schultz, J. Appl. Phys. 91 (2002) 8180.

[132] H. Lemke, C. Echer, G. Thomas, IEEE Trans. Magn. 32 (1996) 4404.

[133] A.J.M. Geursen, J.C.S. Kools, L. de Wit, J.C. Lodder, Appl. Surf. Sci. 96–98 (1996) 887.

[134] C.J. Yang, S.W. Kim, J.S. Kang, J. Magn. Magn. Mater. 188 (1998) 100.

[135] S.Y. Xu, X.J. Huang, C.K. Ong, S.L. Lim, Y.L. Chang, Z. Yang, Z.W. Li, H.B. Nie, J. Magn. Magn. Mater. 222 (2000) 182.

[136] X.J. Huang, S.Y. Xu, C.K. Ong, Z. Yang, L. Si, Y. Li, J. Appl. Phys. 91 (2002) 4666.

[137] F.J. Cadieu, R. Rani, T. Theodoropoulos, L. Chen, J. Appl. Phys. 85 (1999) 5895.

[138] R.A. DeGroot, F.M. Muller, P.G. VanEngen, K.H.J. Buschow, Phys. Rev. Lett. 50 (1983) 2024.

[139] J.A. Cabbalero, Y.D. Park, A. Cabbibo, J.R. Childress, F. Petroff, R. Morel, J. Appl. Phys. 81 (1997) 2740.

[140] W. van Roy, J. de Boeck, B. Brijs, G. Borghs, Appl. Phys. Lett. 77 (2000) 4190.

[141] J. Giapinzakis, C. Grigorescu, A. Klini, A. Manousaki, V. Zorba, J. Androulakis, Z. Viskadourakis, C. Fotakis, Appl. Phys. Lett. 80 (2002) 2716.

[142] A. Semerok et al., Appl. Surf. Sci. 138 (1999) 311.

[143] B.N. Chichkov, C. Momma, S. Nolte, F. von Alvensleben, A. Tünnermann, Appl. Phys. A 63 (1996) 109.

[144] J. Kruger, W. Kautek, Laser Phys. 9 (1999) 30.

[145] I. Ratkay-Traub, I.E. Ferincz, T. Juhasz, R.M. Kurtz, R.R. Krueger, J. Refract. Surg. 19 (2003) 94.

[146] E.G. Gamaly, A.V. Rode, B. Luther-Davies, J. Appl. Phys. 85 (1999) 4213.

[147] P.P. Pronko, P.A. VanRompay, Z. Zhang, J.A. Nees, Phys. Rev. Lett. 83 (1999) 2596.

[148] A.V. Rode, B. Luther-Davies, E.G. Gamaly, J. Appl. Phys. 85 (1999) 4222.

[149] A. Rielly, C. Allmond, S. Watson, J. Gammon, J. Appl. Phys. 93 (2003) 3098.

[150] A.E. Tselev, N.I. Polushkin, Y.K. Verevkin, A.A. Gorbunov, V.N. Petryakov, W. Pompe, Appl. Phys. A 69 (1999) S819.

[151] M. Hirano, K. Kawamura, H. Hosono, Appl. Surf. Sci. 197 (2002) 688.

[152] C. Teichert, M.G. Lagally, L.J. Peticolas, J.C. Bean, J. Tersoff, Phys. Rev. B 53 (1996) 16334.

[153] C. Teichert, J.C. Bean, M.G. Lagally, Appl. Phys. A: Mater. Sci. Process. 67A (1998) 675.

[154] C. Teichert, J. Barthel, H.P. Oepen, J. Kirschner, Appl. Phys. Lett. 74 (1999) 588.

[155] D. Kumar, H. Zhou, T.K. Nath, A.V. Kvit, J. Narayan, Appl. Phys. Lett. 79 (2001) 2817.

[156] S. Ohtsuka, K. Tsunemoto, H. Nagata, S. Tanaka, Appl. Phys. Lett. 61 (1992) 2953.

[157] E. Werwa, A.A. Seraphijn, L.A. Chiu, C. Zhou, K.D. Kolenbrander, Appl. Phys. Lett. 64 (1994) 1821.

[158] J.M. Gonzalez, M.I. Montero, L. Vazquez, J.A.M. Gago, D. Givord, C. de Julian, K. O'Grady, IEEE Trans. Magn. 34 (1998) 1108.

[159] A. Fojtik, A. Henglein, Ber. Bunsenges, Phys. Chem. 97 (1993) 252.

[160] A. Henglein, J. Phys. Chem. 97 (1993) 5457.

[161] J. Muramoto, Y. Nakata, T. Okada, M. Maeda, Jpn. J. Appl. Phys. 36 (1997) L563.

[162] T. Tsuji, T. Kakita, M. Tsuji, Appl. Surf. Sci. 206 (2003) 314.